Mon. Not. R. Astron. Soc. **337,** 1118–1138 (2002)

Bar strengths in spiral galaxies estimated from 2MASS images

Eija Laurikainen★ and Heikki Salo
Department of Physical Sciences, Division of Astronomy, University of Oulu, PO Box 3000, FIN-90014, Finland

Accepted 2002 August 20. Received 2002 August 1; in original form 2002 January 4

ABSTRACT

Non-axisymmetric forces are presented for a sample of 107 spiral galaxies, of which 31 are barred (SB) and 53 show nuclear activity. As a data base we use *JHK* images from the 2 Micron All-sky Survey, and the non-axisymmetries are characterized by the ratio of the tangential force to the mean axisymmetric radial force field, following Buta & Block. Bar strengths have an important role in many extragalactic problems and therefore it is important to verify that the different numerical methods applied for calculating the forces give mutually consistent results. We apply both direct Cartesian integration and a polar grid integration utilizing a limited number of azimuthal Fourier components of density. We find that the bar strength is independent of the method used to evaluate the gravitational potential. However, because of the distance-dependent smoothing by Fourier decomposition, the polar method is more suitable for weak and noisy images. The largest source of uncertainty in the derived bar strength appears to be the uncertainty in the vertical scaleheight, which is difficult to measure directly for most galaxies. On the other hand, the derived bar strength is rather insensitive to the possible gradient in the vertical scaleheight of the disc or to the exact model of the vertical density distribution, provided that the same effective vertical dispersion is assumed in all models. In comparison with the pioneering study by Buta & Block, the bar strength estimate is improved here by taking into account the dependence of the vertical scaleheight on the Hubble type: we find that for thin discs bar strengths are stronger than for thick discs by an amount that may correspond to as much as one bar strength class.

We confirm the previous result by Buta and co-workers showing that the dispersion in bar strength is large among all the de Vaucouleurs optical bar classes. In the near-infrared 40 per cent of the galaxies in our sample have bars (showing constant phases in the $m = 2$ Fourier amplitudes in the bar region), while in the optical band one-third of these bars are obscured by dust. Significant non-axisymmetric forces can also be induced by the spiral arms, generally in the outer parts of the galactic discs, which may have important implications on galaxy evolution. Possible biases of the selected sample are also studied: we find that the number of bars identified drops rapidly when the inclination of the galactic disc is larger than 50°. A similar bias is found in the Third Reference Catalogue of Bright Galaxies, which might be of interest when comparing bar frequencies at high and low redshifts.

Key words: galaxies: active – galaxies: kinematics and dynamics – galaxies: spiral – galaxies: statistics.

1 INTRODUCTION

Bars consist mostly of old stellar populations (de Vaucouleuors 1955; Elmegreen & Elmegreen 1985), which stresses their significance as dynamically important components in galaxies. In fact, a large fraction of galaxies have bars (Block & Wainscoat 1991; Eskridge et al. 2000; Knapen, Shlosman & Peletier 2000; Block et al. 2001), indicating that they must be long-lived phenomena in galaxies. Bars are fundamental in galaxy evolution, suggested to be driving forces for star formation, formation of rings and global spiral density waves, and even for the onset of nuclear activity. When quantified the correlations between bar strength and the other properties of the galaxies can be studied. The wavelength that best traces the dynamical mass is the near-infrared (near-IR), where the obscuration of dust is also less significant than in the optical region. For example, galaxies such as NGC 5195, which are irregular in the optical range may have regular grand-design spiral arms in the near-IR (Block et al. 1994), which emphasizes the importance of a new,

★E-mail: eija.laurikainen@oulu.fi

more dynamical picture of the morphological structure in galaxies. A step toward that direction is the new dust-penetrated classification of galaxies in the near-IR (Block & Puerari 1999; Block et al. 2001; Buta & Block 2001), in which bar strength plays an important role.

As discussed by Buta & Block (2001, BB hereafter) there are many quantitative parameters that can be used to estimate bar strengths, such as bar–interarm contrast (Elmegreen & Elmegreen 1985) or light remaining after the disc and bulge components are subtracted (Seigar & James 1998). The most commonly used method is the maximum ellipticity of a bar – an approach justified by the analytical models of Athanassoula (1992), who showed that the non-axisymmetric forces in the bar correlate with the bar ellipticity. This method has been refined recently by Abraham & Merrifield (2000), who consider both the inner and outer contours of the image to better resolve the ellipticity of a bar. However, the ellipticity is not a full description of bar strength. In fact, a more physical approach has been taken by BB who estimate bar torques by calculating tangential forces in the bar region, also taking into account the underlying axisymmetric potential. Indeed, when refined, the bar torque method is probably the most promising method of estimating bar strengths.

When the bar torque method is finely tuned, future refinements will include the complex bar structures seen in many galaxies; taking more properly into account the vertical scaleheights and their gradients, and taking into account bulge stretch scenarios upon deprojection of the images. In the bar torque method there are different ways of evaluating the gravitational potential and it is important to verify that the different methods give mutually consistent results. For example, BB used the two-dimensional (2D) Cartesian integration method of Quillen, Frogel & Gonzalez (1994), whose new contribution in the potential evaluation was that the vertical density profile of the disc was taken into account in the convolution function. The potential was calculated on a Cartesian grid by applying fast Fourier transform techniques (see also Elmegreen, Elmegreen & Seiden 1989). On the other hand, in our study of IC 4214 (Salo et al. 1999) we evaluated the barred potential by first 'smoothing' the image by calculating the Fourier decomposition of the surface density on a polar grid. In principle, these two methods should give similar results.

In the present study bar strengths are calculated in *JHK* bands for 107 spiral galaxies using the polar method (Salo et al. 1999) for the evaluation of the gravitational potential. The method has been improved by taking into account the recent observational work, showing that bars in early-type galaxies are thicker than in late-type galaxies. Also, the effects of a distance-dependent scaleheight, detected in many boxy/peanut-shaped discs, are estimated. The algorithm of calculating forces is described, the different methods of estimating the gravitational potential are compared and Fourier analysis is applied for bars. Also, biases of the sample are studied and the distributions of bar torques among the de Vaucouleurs' optical bar classes are compared. In future the method will be further developed to better take into account the observational properties of bars and bulges in galaxies. The measurements of this paper have been used in comparisons of bar strengths between active and non-active galaxies by Laurikainen, Salo & Rautiainen (2002).

2 THE SAMPLE SELECTION

A sample of spiral galaxies was selected from the Third Reference Catalogue of Bright Galaxies (de Vaucouleurs et al. 1991, RC3) requiring that $B_T < 12.5$ mag, $cz < 2500$ km s^{-1} and the inclination INC $< 67^\circ$. As a data base we use the 2 Micron All-sky Survey (2MASS). As only approximately 50 per cent of the galaxies in our original sample have images available in 2MASS, the sample in the present form is not magnitude-limited. Some of the weakest images were also eliminated, because bar strengths could not be measured in a reliable manner for them. The final sample consists of 107 spiral galaxies, of which 31 are barred (SB) in RC3, 53 show nuclear activity, 42 are early-type spirals (SO/a-Sb) and the rest of the galaxies belong to late types. For active galaxies we include Seyferts, LINERs and H II/starburst galaxies, the type of activity being taken from the NASA/IPAC Extragalactic Data Base (NED), where the most recent classifications are available.

The frequency of bars in our sample is typical in comparison with other samples of galaxies. Including for barred galaxies both SB and SAB types we find a bar frequency of 62 per cent, which is similar to that obtained by Sellwood & Wilkinson (1993) for field galaxies (60 per cent barred) and by Ho, Filippenko & Sargent (1997) for a magnitude-limited sample ($B_T < 12.5$) of spiral galaxies (59 per cent barred). A somewhat larger fraction of barred galaxies has been found by Hunt & Malkan (1999) for a sample selected by 12-μm radiation (69 per cent barred) and by Moles, Marquez & Pérez (1995) for a magnitude-limited sample extending to $B_T = 13$ mag (68 per cent barred). The numbers of SB and SAB galaxies in our sample are rather similar (29 and 33 per cent). While identifying bars in the near-IR by Fourier techniques (see Section 5.3) the fraction of barred galaxies was found to be 40 per cent.

The fraction of SB galaxies among Seyferts and LINERs in our sample is 30 per cent, being similar to that for the whole sample, in agreement with the bar fractions detected in the samples by Ho et al. (1997) and Mulchaey & Regan (1997). An enhanced frequency of bars is generally associated with H II/starburst galaxies; for example, the fraction of SB galaxies among the Markarian starburst galaxies is 75 per cent (Hunt & Malkan 1999). The bar fraction among H II/starburst galaxies decreases somewhat when weaker nuclear star formation activity is considered: namely, over the whole 12-μm sample by Hunt & Malkan the fraction of SB galaxies is 53 per cent, but concentrating to smaller distances ($cz < 5000$ km s^{-1}), it decreases to 46 per cent. In our sample only two out of 17 H II galaxies are classified as SB, which can be partly understood by the small distances of the galaxies ($\langle cz \rangle = 1200$ km s^{-1}): most probably we are picking the lower end of the nuclear H II luminosity function, where bars may not be the driving forces for nuclear star formation.

The frequency of bars depends strongly on the redshift range studied: at small distances almost all galaxies show nuclear activity at some level (Ho et al. 1997), while the number of strong active nuclei increases with redshift. In our sample 53 per cent of the galaxies have active nuclei in terms of Seyferts, LINERs and H II/starburst galaxies. As we have the same apparent magnitude limit as Ho et al. more H II/starburst galaxies would be expected. The reason why we do not have more H II/starburst galaxies is most probably that NED may not sample the lowest level activity well. The morphological types of Seyferts and LINERs in our sample are peaked at Sab galaxies, which is between the mean morphological types for Seyfert 1 (Sa) and Seyfert 2 (Sb) galaxies (Malkan, Gorjian & Tam 1998), whereas three-quarters of the non-active galaxies belong to late Hubble types.

3 EVALUATION OF THE GRAVITATIONAL POTENTIAL

As in BB, here the bar strengths are also estimated from the magnitude of the non-axisymmetric gravitational perturbation in comparison with the mean axisymmetric radial force field. For

each radius r and azimuth ϕ we calculate the tangential force $F_{\rm T} = \frac{1}{r}\partial\Phi/\partial\phi$ and the radial force $F_{\rm R} = \partial\Phi/\partial r$, and define the relative strength of the perturbation as

$$Q_{\rm T}(r) = F_{\rm T}^{\rm max}(r)/\langle F_{\rm R}(r)\rangle, \tag{1}$$

where the average of the radial force over the azimuth is taken. Following BB the tangential force maxima were calculated separately in four quadrants of the image and the mean of these in each distance is used as the maximum $F_{\rm T}$. In order to obtain a single measure for the strength we use $Q_{\rm b}$, which is the maximum $Q_{\rm T}$ in the bar region. The radial distance where this maximal perturbation takes place is denoted by $r_{Q_{\rm b}}$.

For the force calculation the gravitational potential Φ in the bar region must be evaluated. We assume that the surface density Σ is proportional to the surface brightness obtained from the near-IR image, and that the vertical density distribution follows a model profile $\varrho_z(z)$, normalized to unity when integrated over z. First, it was assumed that the z dependence of the mass density obeys the same formula everywhere in the galaxy (see Section 4.1), in which case the gravitational potential in the central plane of the galaxy can be written as (e.g. Quillen et al. 1994)

$$\Phi(x, y, z=0) = -G\int_{-\infty}^{\infty}\int_{-\infty}^{\infty}\Sigma(x', y')g(x-x', y-y')\,{\rm d}x'\,{\rm d}y', \tag{2}$$

where the integral over the z-direction is included in the convolution function $g(x-x', y-y') \equiv g(\Delta r)$, with $\Delta r^2 = (x-x')^2 + (y-y')^2$, defined as

$$g(\Delta r) = \int_{-\infty}^{\infty}\varrho_z(z)(\Delta r^2 + z^2)^{-1/2}\,{\rm d}z. \tag{3}$$

Several models for $\varrho_z(z)$ were applied, including the exponential model with scaleheight h_z,

$$\varrho_z(z) = \frac{1}{2h_z}\exp(-|z/h_z|), \tag{4}$$

and the often used isothermal sheet model (van der Kruit & Searle 1981),

$$\varrho_z(z) = \frac{1}{2h_{\rm sech\,2}}{\rm sech}^2(z/h_{\rm sech\,2}), \tag{5}$$

where $h_{\rm sech2}$ is the isothermal scaleheight. Usually, when the isothermal model is used, $h_{\rm sech2}$ is set equal to $2h_z$, to yield the same slope at large z as for the exponential model. According to van der Kruit (1988) galactic discs may, however, deviate from an isothermal shape near the galactic plane, in which case a better approximation for the density distribution would be

$$\varrho_z(z) = \frac{1}{\pi h_{\rm sech}}{\rm sech}(z/h_{\rm sech}). \tag{6}$$

In the case of a sech law, Barnaby & Thronson (1992) identify $h_{\rm sech}$ with $(\pi/4)h_z$, to obtain the same central plane density as in the sech^2-law. However, in this study we briefly check the sech-law with $h_{\rm sech} = h_z$, in which case the slope of the vertical profile corresponds to an exponential model at large z. De Grijs, Peletier & van der Kruit (1997) have explored a more general family of fitting functions, which include the above functions as special cases. As will be discussed below the adopted vertical model has rather little influence on the derived forces, provided that appropriately defined scaleheights are used.

In comparison with BB we use a somewhat different method for the evaluation of the gravitational potential, mainly because the 2MASS images used here have a poorer resolution (1arcsec pixel^{-1}) and lower signal-to-noise (S/N) ratio than the images used by BB. Thus, instead of calculating the gravitational potential directly from the image pixels, the images are first 'smoothed' by calculating the Fourier decompositions of the surface densities in different radial zones,

$$\begin{aligned}\Sigma(r,\phi) &= \Sigma_0(r) + \sum_{m=1}^{m=\infty}\Sigma_m(r,\phi)\\ &= A_0(r) + \sum_{m=1}^{m=\infty}A_m(r)\cos\{m[\phi-\phi_m(r)]\}.\end{aligned} \tag{7}$$

The density of each Fourier component is then tabulated separately as a function of radius and azimuth, and for each density component the corresponding potential component is obtained from

$$\Phi_m(r,\phi,z=0) = -G\int_0^{\infty}r'\,{\rm d}r'\int_0^{2\pi}\Sigma_m(r',\phi')g(\Delta r)\,{\rm d}\phi', \tag{8}$$

with $\Delta r^2 = r'^2 + r^2 - 2rr'\cos(\phi'-\phi)$. The integration over the azimuthal direction is carried out using a fast Fourier transform (FFT), whereas in the radial direction a direct summation is used. An azimuthal offset of half a bin is used between the density and the potential locations, and the force components at density locations are obtained from the potential by numerical differentiation. For test purposes, we also applied Cartesian potential evaluation, solving equation (1) with a 2D FFT as in BB. In comparison with direct Cartesian force evaluation the advantage of our polar method is that rather weak and noisy structures can also be measured in a reliable manner, owing to the smoothing implied by Fourier decomposition. Also, it is possible to limit the density to even components, most likely to characterize the non-axisymmetry related to the bar. Our method also gives the different Fourier modes of the potential and force components directly, which are sometimes of interest.

As in BB and Quillen et al. (1994), we made use of the fact that the convolution function $g(\Delta r)$ can be integrated numerically and tabulated as a function of $\Delta r/h$, where h denotes the vertical scalefactor used, so that the integration over the z-direction can be replaced by a much faster interpolation from pre-calculated tables. In addition, since in the polar method only the integration over azimuth is carried out by a FFT, a distance-dependent h can be used: in this case $g(\Delta r/h)$ in equation (8) remains cyclic with $\phi'-\phi$ even if $h = h(r')$. In the Cartesian 2D FFT this cannot be done as the convolution function needs to be cyclic in both $x-x'$ and $y-y'$.

In Fig. 1 we display the convolution functions corresponding to various vertical models. The upper row shows the density profiles and convolution functions corresponding to exponential, sech, and sech^2-model profiles. The difference in $g(\Delta r)$ is significant only for $\Delta r < h_z$. In the lower row of the figure we illustrate the relative insensitiveness of $g(\Delta r)$ for a wider range of $\varrho_z(z)$ models, including the Gaussian model,

$$\varrho_z(z) = \frac{1}{\sqrt{2\pi}h_{\rm gauss}}\exp\left(-\frac{z^2}{2{h_{\rm gauss}}^2}\right), \tag{9}$$

and a uniform slab-model,

$$\varrho_z(z) = \frac{1}{2h_{\rm uni}}, \quad -h_{\rm uni} < z < h_{\rm uni}. \tag{10}$$

In order to make the models comparable, the scalefactors in each case were chosen in a manner that yields the same vertical

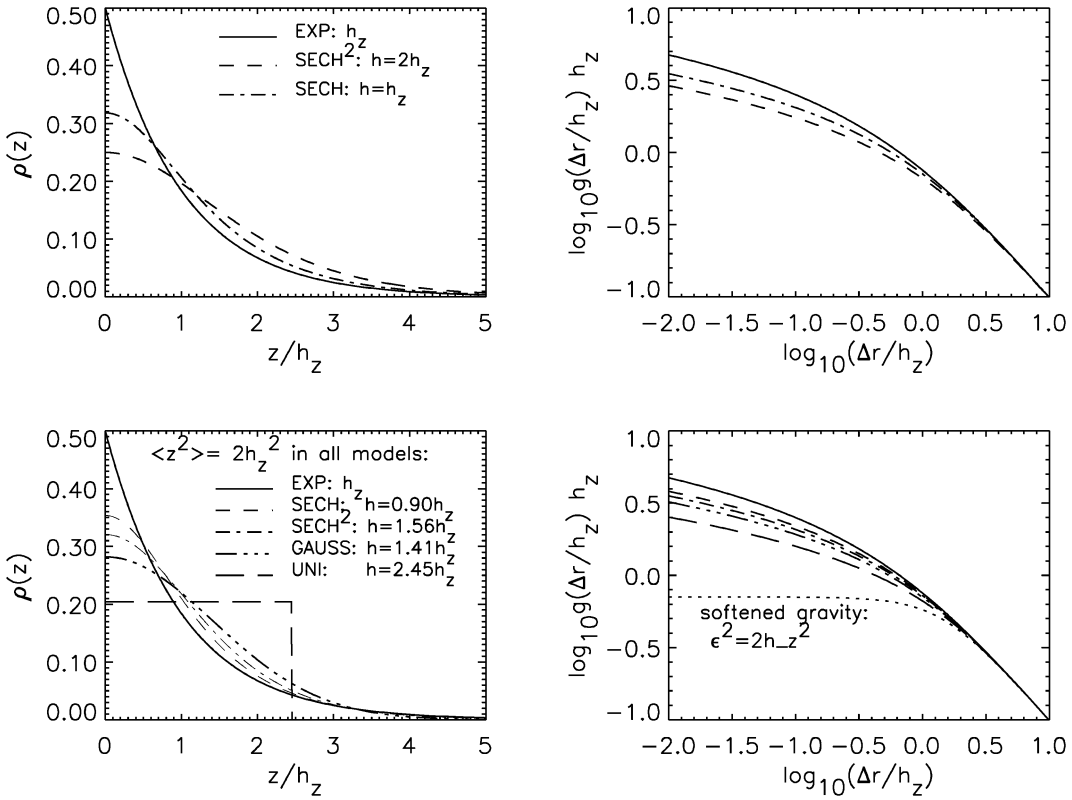

Figure 1. Different models for the vertical density profile are compared. In the upper row the commonly used exponential, sech^2 and sech laws are compared, with the scalefactor h chosen in a manner that yields identical slopes for $z \gg h_z$. The frame on the left-hand side displays the vertical profiles, while on the right-hand side the resulting convolution functions g are shown. These models correspond to those applied in Table 1 for calculation of $Q_{\rm b}$. The lower row compares five different model profiles, also including Gaussian and uniform models. The scalefactors are chosen in a manner that yields the same vertical dispersion in each case. For comparison, the convolution function corresponding to 2D softened gravity is also shown, with softening parameter $\epsilon = \sqrt{\langle z^2 \rangle}$. These same models are applied for the calculation of $Q_{\rm T}$ profiles for NGC 1433 in Fig. 3.

dispersion as the exponential model with $h = h_z$, namely $\langle z^2 \varrho_z(z) \rangle / \langle \varrho_z(z) \rangle = 2{h_z}^2$. In this case

$$
\begin{aligned}
h_{\rm gauss}/h_z &= \sqrt{2}, \\
h_{\rm sech2}/h_z &= \sqrt{24}/\pi, \\
h_{\rm sech}/h_z &= \sqrt{8}/\pi, \\
h_{\rm uni}/h_z &= \sqrt{6}.
\end{aligned}
\tag{11}
$$

As expected, the more peaked the density profile is towards the central plane, the larger the value of $g(\Delta r)$ is when $z \to 0$. In each case $g(\Delta r) \propto 1/\Delta r$ for large Δr, while $g(\Delta r)$ increases logarithmically when $\Delta r \to 0$. In the case of a uniform slab, analytical integration yields

$$
g_{\rm uni} = \frac{1}{h_{\rm uni}} \log \left(\frac{h_{\rm uni} + \sqrt{h_{\rm uni}^2 + \Delta r^2}}{\Delta r} \right), \tag{12}
$$

in agreement with the result of the numerical integration shown in Fig. 1. For comparison, Fig. 1 also displays the case of using 2D softened gravity,

$$
g_{\rm soft} = 1/\sqrt{\Delta r^2 + \epsilon^2}, \quad \text{with } \epsilon^2 = 2h_z. \tag{13}
$$

In conclusion, the convolution function depends very little on the model used for the vertical mass distribution as long as models with the same vertical dispersion are compared. In the next section bar strengths calculated using different vertical models are compared, as well as results obtained by the two different integration methods.

4 TESTING THE ALGORITHM

4.1 Polar versus Cartesian integration

We next investigate our algorithms for force evaluation using NGC 1433 as a test case. For this galaxy Ron Buta has provided us with his high-quality H-band image, with a 1.141-arcsec pixel scale (Buta et al. 2001). Fig. 2 compares our standard polar method, and our Cartesian potential evaluation, where the de-projected image is interpolated to a density array and then a FFT in Cartesian coordinates is applied with a grid resolution ranging from 64×64 to 512×512. In both polar and Cartesian cases the forces were calculated from a region with a radius of $r_{\rm max} = 180$ pixels (205 arcsec). According to Fig. 2 the obtained $Q_{\rm T}$ profiles converge rapidly as more Fourier components are included, or when a finer Cartesian grid is used. The profiles obtained with the two methods also agree well: the maximum $Q_{\rm T}$ agrees to within a few per cent. The only differences appear at large r, where the polar method yields smaller $Q_{\rm T}$. This is caused by distance-dependent smoothing implied by the polar method, whereas in the Cartesian integration the maximum tangential forces for large r are mainly caused by spurious values connected to individual image pixels. Thus, since the outer parts of the galaxy have a low S/N ratio, the smoothing in the polar method is also physically well motivated.

As the polar method is based on calculating Fourier amplitudes for different density components, it is interesting to check how much each component contributes to the total force: in Fig. 2 even

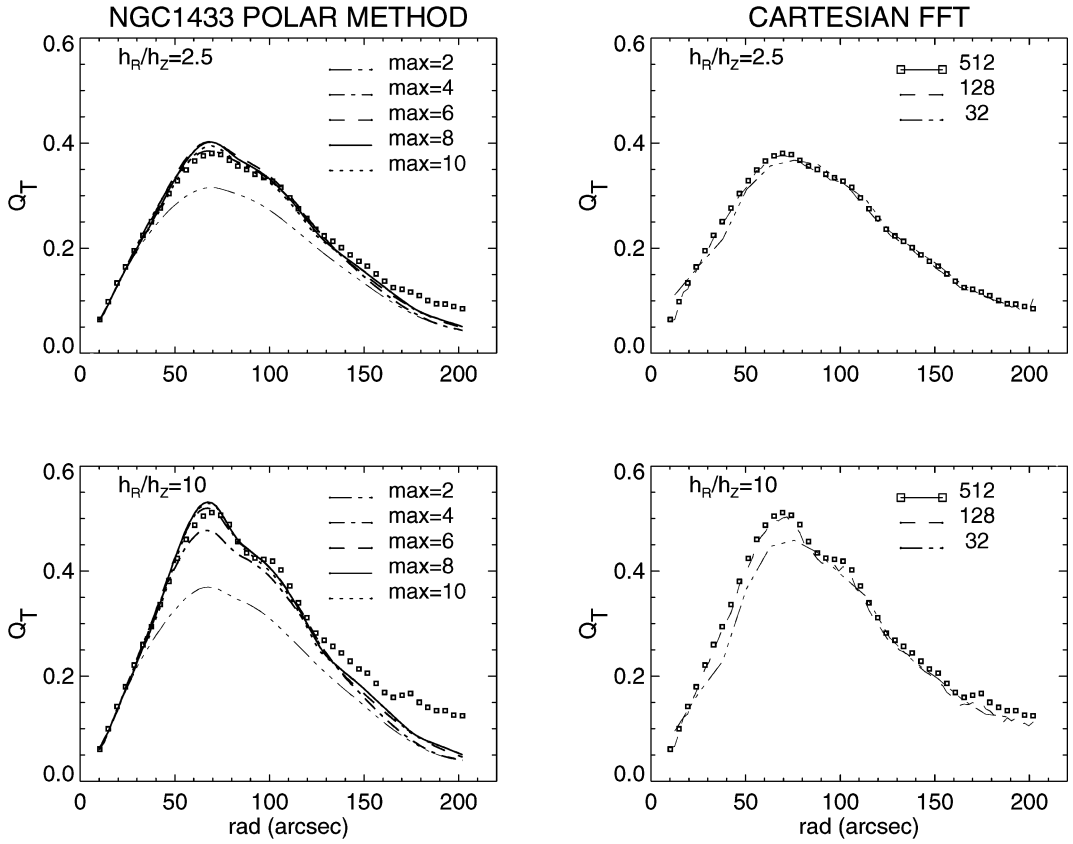

Figure 2. Testing of the calculation method. The left-hand frames show the results of our polar method applied to high-quality H-band image of NGC 1433 (Buta et al. 2001), using different maximal numbers of even Fourier components as indicated in the frame. Fourier components were calculated with 2-pixel wide zones (1 pixel = 1.141 arcsec), and the image was divided into 128 azimuthal bins. In the upper frame $h_r/h_z = 2.5$, typical of early-type galaxies, while the lower frame shows the influence of assuming four times thinner disc. (For $h_r = 45$ arcsec and distance of 11.6 Mpc, the studied h_z values are approximately 1 and 0.25 kpc, respectively.) For comparison, the right-hand frames show results using a Cartesian evaluation of the gravitational potential, with a different number of grid divisions. The results for 512×512 Cartesian grids are also superposed on the left-hand curves.

components up to $m = 10$ are studied. We have used an exponential vertical profile, both with $h_r/h_z = 2.5$, representing an early-type galaxy, and with $h_r/h_z = 10$, to study the effect of assuming a very flat disc. The density amplitudes $m = 2$ and 4 are known to be the strongest in bars, but in bars of early-type galaxies $m = 6$ and 8 may also be significant (Ohta 1996). For NGC 1433 (type Sb) the density amplitudes we find in the H band are fairly similar to those displayed for the I band by Buta (1986), with A_2/A_0 attaining a maximum of ≈ 0.97 at $r = 110$ arcsec, and a secondary maximum of ≈ 0.6 at $r \approx 50$ arcsec. For $m = 4$, 6, 8, 10 the maximum A_m/A_0 are approximately 0.42, 0.22, 0.13, 0.09, respectively, and for the resulting force the maximum appears at $r_{Q_b} = 70$ arcsec, which corresponds to approximately 90 per cent of the bar radius ($R_{bar} = 77$ arcsec, Buta 1986). For $h_r/h_z = 2.5$ approximately 75 per cent of the tangential force is caused by the $m = 2$ density component, and with the inclusion of the $m = 4$ component Q_b increases to 97 per cent of its value obtained by including all even components up to $m = 10$. However, for the case of a flatter galaxy the influence of higher-order Fourier components would become somewhat more important: in the case of $h_r/h_z = 10$, $Q_b = 70$, 90 and 98 per cent of its maximum value, when including the density components up to $m_{max} = 2$, 4, 6, respectively. Thus even in this case the density components above $m = 6$ have fairly little influence. This difference in the relative importance of various Fourier components follows from the fact that planar density variations correspond to force variations only if their planar scale significantly exceeds h_z: smaller h_r/h_z thus suppresses the force variations corresponding to large m.

In the above example the calculation region covered the optical disc of the galaxy well, and the maximum Q_T was obtained at $r_{max}/r_{Q_b} \approx 3$. However, in the case of 2MASS images the outer discs for distant galaxies are sometimes not deep enough. In order to check the influence of the size of the calculation region, a series of integrations with decreasing r_{max} was conducted for NGC 1433. For $r_{max}/r_{Q_b} = 2$ the resulting value of Q_b was only 2 per cent smaller (no shift in r_{Q_b}), whereas for $r_{max}/r_{Q_b} = 1.5$ the reduction was already significant, amounting to 15 per cent. Approximately two-thirds of this reduction is caused by a reduced tangential force, while the remaining part comes from the overestimated radial force owing to disc truncation. However, the location of the Q_T maximum was still fairly little affected (66 arcsec versus 70 arcsec). All of our subsequent force evaluations from 2MASS images are based on images covering a radius at least twice as large as the derived r_{Q_b}.

We also checked the influence of different model functions for the vertical profile on NGC 1433 (Fig. 3). The models correspond to those studied in Fig. 1, each having the same vertical dispersion. As expected, based on the behaviour of the convolution functions, a more centrally peaked vertical profile yields a slightly larger Q_b, although the shape of the Q_T profile is little affected. For

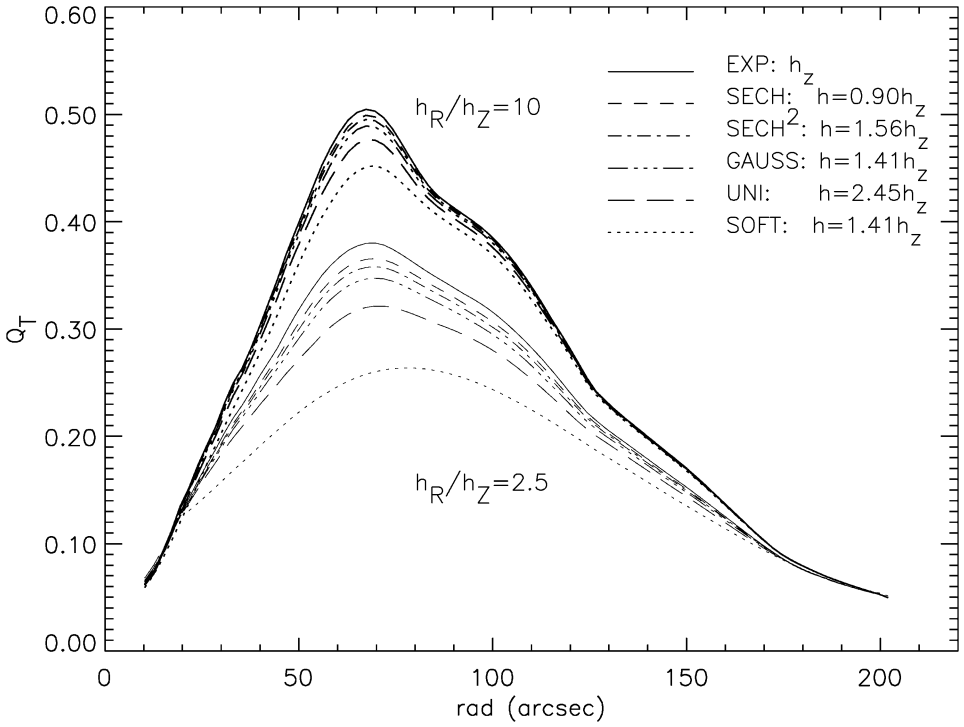

Figure 3. The effect of using different vertical density laws on the obtained $Q_{\rm T}$ profiles for NGC 1433. The density laws correspond to those in the lower row of Fig. 1 (with scalefactors being chosen to yield the same vertical dispersion), and the plot indicates how progressively more peaked vertical density profiles yield stronger non-axisymmetric forces. The two studied values of h_r/h_z are the same as in Fig. 2: for thinner disc the precise form of the density profile is less significant.

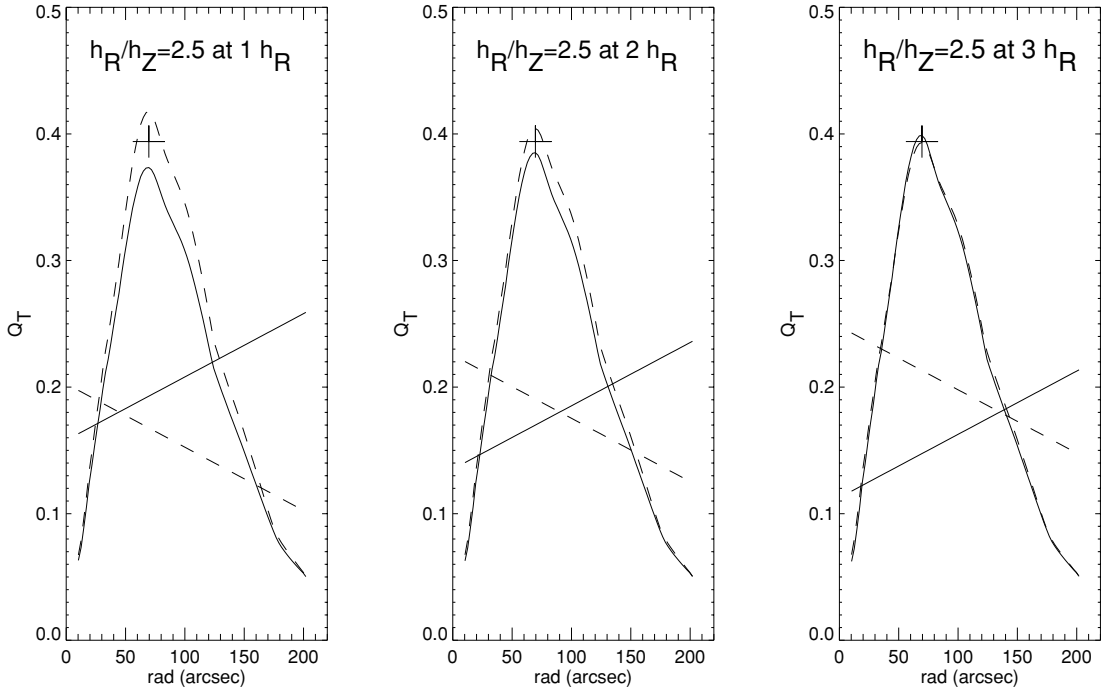

Figure 4. The effect of radius-dependent scaleheight on $Q_{\rm T}(r)$ profiles for NGC 1433. As in Fig. 2, an exponential vertical profile is assumed for each distance, but with either a positive ($\mathrm{d}h_z/\mathrm{d}r = 0.05$, solid curves) or a negative ($\mathrm{d}h_z/\mathrm{d}r = -0.05$, dashed curves) gradient of the vertical scaleheight with distance. Three different cases are studied, where $h_r/h_z = 2.5$, either at $r = 1$, 2, or $3h_r$. The lines indicate the vertical scaleheight profile in each case, with h_z multiplied by 0.01. According to Schwarzkopf & Dettmar (2001), the disc thickness often increases with radius, and $\mathrm{d}h_z/\mathrm{d}r = 0.05$ corresponds to the maximum value observed for early types. Negative gradients are also studied, to emphasize the smallness of the expected maximal effect of vertically dependent h_z. For comparison, the crosses indicate the peak of the $Q_{\rm T}$ profile in the case of constant $h_r/h_z = 2.5$. The polar method is used.

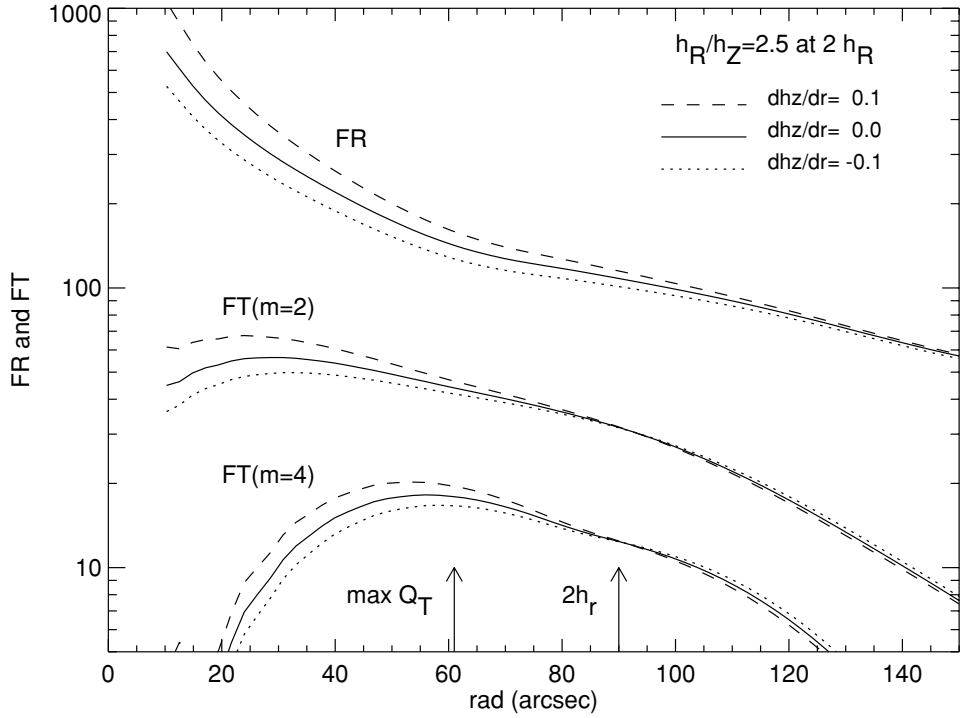

Figure 5. A more detailed comparison of the effects of distance-dependent h_z, corresponding to the middle frame in Fig. 4, except that twice as large positive and negative gradients are studied, together with the case of constant h_z. The mean radial force profile is shown, together with the $m=2$ and 4 Fourier amplitudes of the tangential force components (forces are in arbitrary units). As expected, tangential force components are increased in regions where the scaleheight is reduced. The same is also true for the radial force, which, however, is even more strongly affected in the region of maximal F_T/F_R ratio, explaining the slightly reduced Q_T in the case of a positive dh_z/dr gradient.

Table 1. For the test galaxies: bar strengths and the parameters used in the calculation.

Galaxy	PA	INC	Dist. (Mpc)	Q_b (sech^2)	Q_b (sech)	Q_b (exp)	Q_b (BB)
Maffei2	23	65.1	3.4	0.33	0.34	0.35	0.27 ± 0.03
E565-G11	73	33.0	63.0	0.39	0.41	0.42	0.28 ± 0.03
E566-G24	67	42.5	45.0	0.36	0.37	0.39	0.27 ± 0.04
N309	175	33.7	75.5	0.26	0.27	0.28	0.11 ± 0.02
N1300	106	48.6	18.8	0.55	0.58	0.60	0.42 ± 0.06
N1637	15	35.6	8.9	0.20	0.21	0.22	0.09 ± 0.03
N2543	45	54.9	32.9	0.31	0.33	0.35	0.28 ± 0.05
N3081	123	33.0	32.5	0.28	0.28	0.29	0.17 ± 0.02
N4548	150	37.4	16.8	0.38	0.39	0.40	0.44 ± 0.03
N4653	30	29.4	39.1	0.20	0.22	0.23	0.04 ± 0.01
N5371	8	37.4	34.1	0.19	0.20	0.21	0.19 ± 0.02
N5905	135	48.6	42.5	0.43	0.44	0.45	0.43 ± 0.05
N7479	25	40.6	32.4	0.73	0.76	0.79	0.63 ± 0.08

early-type galaxies with $h_r/h_z=2.5$, the difference in Q_b between the exponential and uniform models is 15 per cent, which is much less than the difference between the cases $h_r/h_z=2.5$ and 10 for a fixed vertical model function. Also, while comparing more realistic vertical models, namely the exponential and the isothermal model, Q_b is affected only by 5 per cent. In general, when the vertical extent of the disc is reduced, the exact form of the vertical density law becomes less important. In the limit of very large h_r/h_z the difference between including a three-dimensional (3D) vertical profile and the use of softening in 2D force evaluation also becomes small, in agreement with Salo et al. (1999). However, for large disc thicknesses ($h_r/h_z=2.5$), the use of softened gravity severely underestimates Q_b.

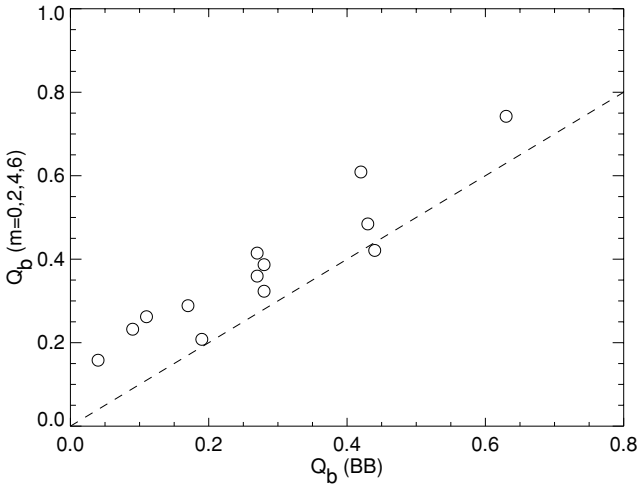

Figure 6. Bar strength measurements by BB and by us are compared for 13 galaxies in the H band. In both measurements the same orientation parameters were used and the vertical mass distribution was approximated by an exponential profile with $h_z=325$ kpc ($H_0=75$ km s^{-1} Mpc^{-1}). The $m=0$, 2, 4, 6 Fourier components of density were included, and calculated for radial annuli with a width of 2 arcsec. In the azimuthal direction 128 divisions were used in all cases. No softening was used in our potential evaluation.

4.2 Distant-dependent disc thickness

As many galaxies have boxy/peanut-shaped structures, for which the vertical thickness is found to increase towards the outer parts of the galaxies, we also studied a case with a distant-dependent

Table 2. General properties of theAuthor: ["] – should this be arcsec or Mpc? galaxies in the sample.

pgc	NGC	T_m	B_T	PA	INC	Dist. (Mpc)	h_R (arcsec)	act
2 081	N157	.SXT4..	11.00	40	49.8	20.9	35.8 (V)(6)	
2 437	N210	.SXS3..	11.60	160	48.6	20.3	15*	
3 051	N278	.SXT3..	11.47	–	17.3	11.8	13*	
3 089	N289	.SBT4..	11.72	130	44.9	19.4	14.0 (V)(6)	
5 619	N578	.SXT5..	11.44	110	50.9	19.5	38*	
5 818	N598	.SAS6..	6.27	23	53.9	0.7	533.3 (V)(6)	H II
7 525	N772	.SAS3..	11.09	125 (1)	50.2 (1)	32.3	56*	
9 057	N908	.SAS5..	10.83	75	64.1	17.8	45*	
10 122	N1042	.SXT6..	11.56	155	12.2	16.7	57.9 (V)(6)	
10 266	N1068	RSAT3..	9.61	70	31.7	14.4	21.4*	Sy1/Sy2
10 464	N1084	.SAS5..	11.31	25	55.8	17.1	19*	
10 488	N1097	.SBS3..	10.23	130	47.5	14.5	39*	Sy1
10 496	N1087	.SXT5..	11.46	5	52.9	19.0	20.1 (V)(6)	
11 479	N1187	.SBR5..	11.34	130	42.2	16.3	23.3 (V)(6)	
11 819	N1232	.SXT5..	10.52	108	29.4	21.1	42*	
12 007	N1255	.SXT4..	11.40	117	50.9	19.9	29.8 (V)(6)	
12 412	N1300	.SBT4..	11.11	106	48.6	18.8	76.6 (V)(6)	
12 431	N1302	RSBR0..	11.60	–	17.3	20.0	65*	
12 626	N1309	.SAS4*.	11.97	45	21.0	26.0	14*	
13 059	N1350	PSBR2..	11.16	0	57.5	16.9	31*	Sy
13 255	N1367	.SXT1..	11.57	135	46.2	17.1	50.6 (V)(6)	
13 368	N1385	.SBS6..	11.45	165	55.0 (5)	17.5	29.2 (V)(6)	
13 434	N1398	PSBR2..	10.57	100	40.7	16.1	29.4 (V)(6)	Sy
13 602	N1425	PSBR2..	11.29	129	63.5	17.4	46.5 (V)(6)	Sy
14 814	N1559	.SBS6..	11.00	64	60.0	14.3	31*	
15 821	N1637	.SXT5..	11.47	15	35.6	8.9	38.0*	
16 709	N1792	.SAT4..	10.87	137	59.9	13.6	34*	
16 779	N1808	RSXS1..	10.74	133	53	10.8	26.9 (I)(4)	Sy2
16 906	N1832	.SBR4..	11.96	10	48.6	23.5	15.3 (V)(6)	
18 258	N2139	.SXT6..	11.99	0	0	22.4	19.7 (V)(6)	
18 602	N2196	PSAS1..	11.82	35	39.1	28.8	27.2 (V)(6)	
19 531	N2280	.SAS6..	10.90	163	60.7	23.2	45.1 (V)(6)	
25 069	N2655	.SXS0..	10.96	–	33.7	24.4	52*	Sy2
26 259	N2835	.SBT5..	11.01	8	48.6	10.8	62.6 (V)(6)	
26 512	N2841	.SAR3*.	10.09	147	64.1	12.0	45.0 (V)(6)	Sy1/L
27 077	N2903	.SXT4..	9.68	17	60.0(4)	6.3	54.5 (V)(6)	H II
27 777	N2964	.SXR4*.	11.99	97	56.7	25.9	21.2 (V)(6)	H II
28 120	N2976	.SA.5P.	10.82	141 (1)	55.2 (1)	2.1	45*	H II
28 316	N2985	PSAT2..	11.18	2 (1)	36.9 (1)	22.4	35*	L
28 630	N3031	.SAS2..	7.89	157	58.3	1.4	157.5 (V)(6)	Sy1.8/L
29 146	N3077	.I.0.P.	10.61	45	33.7	2.1	44*	H II
30 087	N3184	.SXT6..	10.36	135	21.1	8.7	74.0 (V)(6)	H II
30 445	N3227	.I.0.P.	11.10	155	47.5	23.4	23.6 (V)(6)	H II
31 650	N3310	.SXR4P.	11.15	–	39.1	18.7	123.0 (V)(6)	H II
31 883	N3338	.SAS5..	11.64	100	51.9	22.8	25.3 (V)(6)	
32 183	N3359	.SBT5..	11.03	170	52.9	19.2	36*	H II
33 166	N3486	.SXR5..	11.05	111 (1)	24.5 (1)	7.4	36*	Sy2
33 371	N3504	RSXS2..	11.82	–	39.1	26.5	21.9 (V)(6)	H II
33 390	N3507	.SBS3..	11.73	90 (2)	21.6 (2)	19.8	25.0 (K)(5)	L
33 550	N3521	.SXT4..	9.83	163	57.0 (5)	7.2	37.7 (I)(4)	L
34 298	N3596	.SXT5.	11.95	139 (2)	28.4 (2)	23.0	27.9 (B)(5)	
35 164	N3675	.SAS3..	11.00	2 (1)	57.3 (1)	12.8	34*	
35 193	N3681	.SXR4..	11.90	103 (2)	32.9 (2)	24.2	14.0 (K)(5)	
35 268	N3686	.SBS4..	11.89	13.1 (2)	41.4 (2)	23.5	27.6 (B)(5)	
35 616	N3718	.SBS1P.	11.59	173 (1)	52.0 (1)	17.0	41.4 (V)(6)	Sy1
35 676	N3726	.SXR5..	10.91	10.0	46.4	17.0	–	
36 921	N3898	.SAS2..	11.60	107	53.9	21.9	37.8 (V)(6)	H II/L
37 773	N4027	.SBS8..	11.66	167	40.7	25.6	25.3 (V)(6)	
37 999	N4041	.SAT4*.	11.88	–	21.1	22.7	17*	
38 150	N4062	.SAS5..	11.90	100 (1)	65.8 (1)	9.7	24.7 (V)(6)	H II
38 739	N4151	PSXT2*.	11.50	50 (7)	16.3 (9)	15.5	36*	Sy1.5
39 578	N4254	.SAS5.	10.44	40	29.4	16.8	34.8 (V)(6)	

Table 2 – *continued*

pgc	NGC	T_m	B_T	PA	INC	Dist. (Mpc)	h_R (arcsec)	act
39 724	N4274	RSBR2..	11.34	102 (1)	67.0 (1)	9.7	56.9 (V)(6)	
39 907	N4293	RSBS0..	11.26	72	65.0 (3)	17.0	42.9 (V)(6)	L
40 097	N4314	.SBT1..	11.43	–	27.0	9.7	43.3*	L
40 153	N4321	.SXS4..	10.05	153 (2)	27.1 (2)	16.8	64.0 (B)(5)	H II/L
40 614	N4394	RSBR3..	11.73	–	25.0 (3)	16.8	33.0 (V)(6)	L
40 692	N4414	.SAT5.	10.96	161 (1)	45.6 (1)	9.7	27.6 (V)(6)	
41 024	N4450	.SAS2..	10.90	171 (2)	46.4 (2)	16.8	44.8 (K)(5)	L
41 333	N4490	.SBS7P.	10.22	125	60.7	9.3	38.4 (V)(6)	
41 517	N4501	.SAT3..	10.36	140	57.5	16.8	47.0 (V)(6)	Sy2
41 934	N4548	.SBT3..	10.96	150	37.4	16.8	28.7 (V)(6)	Sy/L
42 089	N4569	.SXT2..	10.26	23	62.8	16.8	73.5 (V)(6)	Sy/L
42 575	N4618	.SBT9..	11.22	25	35.6	8.2	60*	H II
42 833	N4651	.SAT5..	11.39	73.9 (2)	47.9 (2)	16.8	25.1 (B)(5)	L
42 857	N4654	.SXT6..	11.10	128	57.0 (3)	16.8	39.8 (V)(6)	
43 186	N4689	.SAT4..	11.60	155	40.0 (3)	16.8	38.9 (V)(6)	
43 238	N4691	RSBS0P.	11.66	15	35.6 (4)	22.5	35.8 (V)(6)	
43 321	N4699	.SXT3..	10.41	45	46.2	25.7	–	Sy
43 495	N4736	RSAR2..	8.99	105	35.6	4.3	84.3 (V)(6)	L
43 507	N4731	.SBS6..	11.90	85	60.7	25.9	39*	
43 671	N4753	.I.0 \ ldots	10.85	80	62.1	15.1	46*	
44 182	N4826	RSAT2..	9.36	115	57.	4.1	61.9 (V)(6)	Sy2
45 165	N4941	RSXR2*.	12.43	15	57.5	6.4	21.6 (V)(6)	Sy2
45 749	N5005	.SXT4..	10.61	67 (1)	65.0	21.3	33.0 (V)(6)	Sy2
45 948	N5033	.SAS5..	10.75	173 (1)	60.0 (1)	18.7	731.6 (V)(6)	Sy1.9
46 247	N5054	.SAS4..	11.67	155	54.0 (4)	27.3	40.3 (I)(4)	
46 400	N5068	.SXT6..	10.52	110	29.4	6.7	39.3 (V)(6)	
47 404	N5194	.SAS4P.	8.96	170 (8)	20.0 (8)	9.3	107.5 (V)(6)	H II/Sy2.5
47 413	N5195	.I.0.P.	10.45	90 (9)	30.0 (9)	7.7	29*	L
48 171	N5247	.SAS4..	10.50	20	29.4	22.2	62*	
50 063	N5457	.SXT6..	8.31	–	21.1	5.4	143.4 (V)(6)	
52 412	N5713	.SXT4P.	12.18	10	27.0	30.4	13.8 (V)(6)	
55 588	N5962	.SAR5..	11.98	96.1 (2)	44.8 (2)	31.8	17.9 (B)(5)	H II
56 219	N6015	.SAS6..	11.69	28 (1)	61.3 (1)	17.5	37.1 (V)(6)	H II
58 477	N6217	RSBT4.	11.79	150	33.7	23.9	13.2 (V)(6)	Sy2
61 742	N6643	.SAT5..	11.73	40 (1)	60.0 (1)	25.5	27.7 (V)(6)	
68 096	N7217	RSAR2..	11.02	95	33.7	16.0	26.9 (V)(6)	Sy
68 165	N7213	.SAS1*.	11.01	–	26.9	22.0	82*	Sy1.5
69 253	N7314	.SXT4..	11.88	3	62.8	18.3	–	Sy1.9
69 327	N7331	.SAS3..	10.35	170 (1)	62.6 (1)	14.3	89.4 (V)(6)	L
70 419	N7479	.SBS5..	11.60	40.5 (2)	39.6 (2)	32.4	50.7 (B)(5)	Sy2/L
70 714	N7513	PSBS3P.	11.39	108	48.6	21.3	55*	
71 047	N7606	.SAS3..	11.51	146 (1)	67.7 (1)	28.9	43*	
72 009	N7723	.SBR3..	11.94	35	47.5	23.7	19*	
72 060	N7727	.SXS1P.	11.50	35	40.7	23.3	–	
72 237	N7741	.SBS6..	11.84	170 (2)	45.6 (2)	12.3	52.7 (B)(5)	

Notes. (1) Heraudeau & Simien (1996). (2) de Jong & van der Kruit (1994). (3) Yasuda, Okamura & Fukugita (1995). (4) Roth (1994). (5) de Jong (1996). (6) Baggett et al. (1998). (7) Sanchez-Portal et al. (2000). (8) Tully (1974). (9) Smith et al. (1990).
*Estimated from 2MASS images. **Estimate from the Digitized Sky Survey plate.

vertical scaleheight. Radial distributions of Q_T were calculated for NGC 1433 using an exponential density model, when h_z was assumed to have a mean value and a gradient typical for early-type galaxies (see Section 5.1). As shown in Fig. 4 the vertical density gradient has a fairly small effect on the bar strength: in comparison with the case where a constant h_z was assumed, a gradient of 0.05 in h_z affects Q_T at maximum by only by 4 per cent. In the figure three cases are demonstrated, showing how the location of the mean vertical thickness affects Q_T measurement. In comparison with a constant vertical scaleheight, a radially increasing h_z typically slightly reduces the derived bar strength. This is caused by two competitive effects: on one hand the tangential force increases in the region where the vertical scaleheight is reduced, but at the same time the axisymmetric radial force is also increased in the same region (see Fig. 5).

In interacting galaxies gradients of the vertical scaleheights are generally larger than for normal galaxies, and contrary to normal galaxies, may also appear in late-type systems. Therefore, we also studied some cases, where the h_z gradient was twice as large as for normal galaxies. For $h_r/h_z = 2.5$ the effect of the gradient on Q_b was

Table 3. Q_b, r_{Q_b}, ϵ and r_ϵ for galaxies with classical bars in the near-IR.

pgc	Q_H	r_H (arcsec)	Q_J	r_J (arcsec)	Q_K	r_K (arcsec)	Length (arcsec)	ϵ	r_ϵ (arcsec)
3 089	0.15 ± 0.00	13	0.14 ± 0.00	15	0.17 ± 0.03	15	20	0.39	20.28
10 266	0.15 ± 0.01	11	0.16 ± 0.02	11	0.12 ± 0.01	11	25	0.43	14.96
10 488	0.24 ± 0.01	79	0.24 ± 0.02	79	0.23 ± 0.01	77	120	0.58	94.72
10 496	0.42 ± 0.00	11	0.43 ± 0.01	11	0.44 ± 0.01	11	22	0.63	24.26
11 479	0.19 ± 0.03	29	0.19 ± 0.02	31	0.21 ± 0.03	27	40	0.55	41.42
12 412	0.40 ± 0.03	61	0.38 ± 0.01	59	0.41 ± 0.04	59	80	0.71	68.77
12 431	0.09 ± 0.02	19	0.09 ± 0.01	19	0.09 ± 0.04	19	30	0.35	28.06
13 059	0.29 ± 0.01	69	0.30 ± 0.00	71	0.30 ± 0.00	69	110	0.62	77.30
13 368	0.37 ± 0.01	35	0.35 ± 0.02	35	0.35 ± 0.02	11	45	0.70	9.91
13 434	0.20 ± 0.00	39	0.21 ± 0.01	39	0.20 ± 0.00	39	60	0.54	49.76
13 602	0.16 ± 0.00	11	0.15 ± 0.01	11	0.15 ± 0.01	11	25	0.48	4.73
14 814	0.30 ± 0.02	11	0.27 ± 0.02	13	0.24 ± 0.00	13	15	0.51	13.58
15 821	0.20 ± 0.05	19	0.23 ± 0.00	18	0.24 ± 0.04	17	25	0.56	24.74
16 906	0.23 ± 0.01	13	0.23 ± 0.00	15	0.22 ± 0.01	13	20	0.49	18.46
18 258	0.35 ± 0.01	7	0.33 ± 0.01	5	0.35 ± 0.07	7	25	0.56	0.00
26 259	0.28 ± 0.01	15	0.31 ± 0.00	11	0.38 ± 0.01	15	30	0.58	33.18
27 077	0.26 ± 0.05	61	0.25 ± 0.01	63	0.27 ± 0.00	61	75	0.65	65.81
27 777	0.32 ± 0.00	21	0.33 ± 0.01	21	0.33 ± 0.01	23	30	0.63	26.31
32 183	0.46 ± 0.05	11	0.42 ± 0.01	11	0.45 ± 0.03	11	55	0.65	9.46
33 371	0.26 ± 0.02	27	0.27 ± 0.03	29	0.26 ± 0.02	29	45	0.63	30.91
33 390	0.19 ± 0.04	17	0.21 ± 0.00	21	0.20 ± 0.06	21	20	0.44	20.99
35 268	0.33 ± 0.01	11	0.28 ± 0.02	13	0.30 ± 0.01	11	29	0.59	22.25
35 616	0.12 ± 0.01	65	0.16 ± 0.02	60	0.14 ± 0.01	60	80	0.38	50.00
37 773	0.50 ± 0.01	11	0.51 ± 0.02	11	0.48 ± 0.02	11	20	0.67	7.58
37 999	0.13 ± 0.02	11	0.08 ± 0.00	11	0.09 ± 0.01	11	20	0.33	6.07
38 739	0.16 ± 0.02	67	0.18 ± 0.03	67	0.14 ± 0.01	67	100	0.52	75.72
39 724	0.31 ± 0.03	45	0.31 ± 0.00	41	0.31 ± 0.02	45	100	0.65	66.93
39 907	0.22 ± 0.06	47	0.22 ± 0.01	49	0.21 ± 0.02	47	90	0.50	60.00
40 097	0.33 ± 0.01	47	0.33 ± 0.00	45	0.34 ± 0.00	45	88	0.68	67.71
40 614	0.22 ± 0.01	29	0.21 ± 0.00	27	0.22 ± 0.01	25	65	0.61	43.26
41 024	0.13 ± 0.01	39	0.13 ± 0.01	39	0.17 ± 0.01	41	60	0.41	46.65
41 934	0.33 ± 0.02	49	0.32 ± 0.01	47	0.32 ± 0.00	45	70	0.62	76.98
42 575	0.40 ± 0.03	10	0.36 ± 0.03	11	0.36 ± 0.01	13	45	0.65	16.72
43 238	0.61 ± 0.01	11	0.59 ± 0.01	13	0.63 ± 0.00	11	60	0.77	17.97
43 507	1.19 ± 0.10	23	1.07 ± 0.00	25	1.27 ± 0.02	25	100	0.86	0.00
46 400	0.43 ± 0.03	11	0.41 ± 0.01	13	0.48 ± 0.04	13	52	0.65	20.00
47 413	0.14 ± 0.01	39	0.15 ± 0.00	39	0.13 ± 0.01	41	48	0.46	51.49
52 412	0.37 ± 0.04	11	0.39 ± 0.05	13	0.39 ± 0.02	13	28	0.57	20.21
58 477	0.36 ± 0.01	29	0.40 ± 0.01	25	0.40 ± 0.04	29	40	0.69	35.98
70 419	0.63 ± 0.03	37	0.62 ± 0.02	39	0.65 ± 0.04	43	70	0.78	49.71
70 714	0.46 ± 0.02	17	0.41 ± 0.01	25	0.46 ± 0.01	20	55	0.76	37.84
72 009	0.30 ± 0.02	16	0.28 ± 0.03	15	0.31 ± 0.01	17	28	0.64	20.20
72 237	0.64 ± 0.02	11	0.70 ± 0.02	16	0.70 ± 0.05	13	70	0.77	0.00

still unimportant with Q_b being reduced by only 3 per cent. Thin discs were even less affected: for $h_r/h_z = 10$ we found that while adding a gradient of 0.03, Q_b was unchanged. We can safely conclude that the vertical scaleheight gradient, typical for boxy/peanut-shaped bars, does not significantly affect the bar strength.

4.3 Comparison with BB

We next compare our results with those obtained by BB. Bar strengths for 13 galaxies in the sample by BB were calculated in H band, using the same orientation parameters as used in BB (see Table 1). Also, following BB the vertical mass distribution was approximated by an exponential function with $h_z = 325$ kpc, which is the scaleheight of the disc in the Milky Way. As shown in Fig. 6, there is a small shift toward somewhat larger Q_b in our measurements, but generally the agreement between the two measurements is quite good. No softening was used in our potential evaluation. A possible cause of the small difference is that some form of additional gravity softening was included in the potential evaluation in BB, besides using a vertically extended density model. This possibility is suggested by the form of the convolution function $g(r)$ shown in fig. 2 in Quillen et al. (1994) – the method used by BB. In comparison with our $g(r)$ (Fig. 1), their function seems to attain a constant value for $\Delta r/h \to 0$, much like our curve for softened gravity. Nevertheless, no explicit gravity softening was mentioned in Quillen et al. so it is not clear whether this is the cause of the difference. It is also worth noticing that the comparison was made using 2MASS images, many of which were of poorer quality than the images used by BB. In Table 1 we also show that the vertical density model barely affects the derived bar strength.

Table 4. Bar strengths for galaxies without classical bars.

pgc	Q_H	r_H (arcsec)	Q_J	r_J (arcsec)	Q_K	r_K (arcsec)	Comment
2 081	0.29 ± 0.11	33	0.26 ± 0.00	31	0.26 ± 0.01	35	S
2 437	0.12 ± 0.00	33	0.12 ± 0.01	33	0.11 ± 0.00	33	BM
3 051	0.06 ± 0.02	23	0.06 ± 0.01	25	0.06 ± 0.01	23	
5 619	0.32 ± 0.01	11	0.28 ± 0.01	11	0.33 ± 0.08	11	BM
5 818	0.24 ± 0.00	49	0.25 ± 0.04	35	0.29 ± 0.00	35	BM
7 525	0.10 ± 0.02	33	0.10 ± 0.02	35	0.12 ± 0.00	35	
9 057	0.18 ± 0.02	71	0.19 ± 0.00	67	0.17 ± 0.02	61	S
10 122	0.38 ± 0.00	25	0.35 ± 0.06	23	0.38 ± 0.02	25	BM
10 464	0.18 ± 0.02	29	0.18 ± 0.01	33	0.19 ± 0.03	33	B
11 819	0.17 ± 0.01	11	0.16 ± 0.01	11	0.20 ± 0.03	11	BM
12 007	0.15 ± 0.02	25	0.15 ± 0.02	20	0.18 ± 0.03	25	S
12 626	0.15 ± 0.06	15	0.12 ± 0.02	15	0.14 ± 0.02	15	B
13 255	0.12 ± 0.02	21	0.12 ± 0.00	21	0.15 ± 0.00	23	BM
16 709	0.25 ± 0.00	33	0.24 ± 0.00	33	0.26 ± 0.00	33	S
16 779	0.25 ± 0.00	69	0.27 ± 0.00	67	0.23 ± 0.00	71	BM
18 602	0.07 ± 0.00		0.09 ± 0.02		0.10 ± 0.04		
19 531	0.17 ± 0.02	45	0.17 ± 0.02	45	0.17 ± 0.03	45	BM
25 069	0.12 ± 0.01		0.13 ± 0.01		0.13 ± 0.03		B
26 512	0.18 ± 0.01	13	0.19 ± 0.01	13	0.19 ± 0.01	13	BM
28 120	0.30 ± 0.01	57	0.30 ± 0.02	61	0.35 ± 0.01	63	BM
28 316	0.03 ± 0.03		0.02 ± 0.01		0.02 ± 0.02		
28 630	0.06 ± 0.02		0.06 ± 0.02		0.06 ± 0.02		
29 146	0.07 ± 0.03		0.09 ± 0.01		0.07 ± 0.03		
30 087	0.16 ± 0.01	45	0.15 ± 0.01	45	0.15 ± 0.01	45	S
30 445	0.18 ± 0.07	49	0.18 ± 0.01	41	0.19 ± 0.00	53	B
31 650	0.06 ± 0.01		0.04 ± 0.00		0.07 ± 0.00		
31 883	0.12 ± 0.01	45	0.14 ± 0.05	49	0.16 ± 0.03	45	S
33 166	0.16 ± 0.00	17	0.15 ± 0.00	60	0.16 ± 0.00	60	BM
33 550	0.02 ± 0.00		0.06 ± 0.01		0.06 ± 0.01		
34 298	0.16 ± 0.01	23	0.16 ± 0.04	19	0.16 ± 0.02	34	S
35 164	0.04 ± 0.01		0.04 ± 0.00		0.04 ± 0.03		S
35 193	0.25 ± 0.01	8	0.21 ± 0.02	9	0.23 ± 0.01	8	BM
35 676	0.33 ± 0.04	23	0.30 ± 0.01	27	0.30 ± 0.05	29	BM
36 921	0.03 ± 0.02		0.02 ± 0.02		0.02 ± 0.00		
38 150	0.14 ± 0.03	47	0.09 ± 0.00	50	0.13 ± 0.02	47	BM
39 578	0.12 ± 0.01	19	0.13 ± 0.01	23	0.13 ± 0.02	21	S
40 153	0.20 ± 0.07	59	0.20 ± 0.02	59	0.22 ± 0.02	61	S
40 692	0.11 ± 0.01		0.11 ± 0.00		0.11 ± 0.00		S
41 333	0.25 ± 0.01	73	0.25 ± 0.01	73	0.25 ± 0.01	73	BM
41 517	0.07 ± 0.01		0.07 ± 0.00		0.07 ± 0.00		
42 089	0.15 ± 0.01	61	0.14 ± 0.01	61	0.17 ± 0.01	59	BM
42 833	0.05 ± 0.01	17	0.05 ± 0.01	13	0.12 ± 0.01	19	BM
42 857	0.14 ± 0.02		0.14 ± 0.00		0.14 ± 0.00		S
43 186	0.03 ± 0.01		0.03 ± 0.00		0.04 ± 0.02		
43 321	0.04 ± 0.01		0.04 ± 0.02		0.04 ± 0.01		
43 495	0.02 ± 0.01		0.02 ± 0.01		0.02 ± 0.01		
43 671	0.21 ± 0.00		0.20 ± 0.00		0.20 ± 0.01		B
44 182	0.13 ± 0.01		0.12 ± 0.00		0.13 ± 0.00		
45 165	0.05 ± 0.00		0.04 ± 0.02		0.04 ± 0.05		
45 749	0.16 ± 0.01	25	0.15 ± 0.01	25	0.17 ± 0.01	28	BM
45 948	0.07 ± 0.04		0.04 ± 0.03		0.05 ± 0.05		
46 247	0.15 ± 0.03	45	0.16 ± 0.04	47	0.12 ± 0.05	45	S
47 404	0.16 ± 0.00	113	0.17 ± 0.01	113	0.17 ± 0.00	111	S
48 171	0.25 ± 0.04	50	0.27 ± 0.02	61	0.24 ± 0.05	61	S
50 063	0.10 ± 0.02		0.14 ± 0.02		0.15 ± 0.02		S
55 588	0.22 ± 0.03	13	0.21 ± 0.00	15	0.26 ± 0.02	15	BM
56 219	0.08 ± 0.01		0.09 ± 0.04		0.09 ± 0.01		
61 742	0.16 ± 0.10		0.20 ± 0.01		0.20 ± 0.01		B
68 096	0.05 ± 0.01		0.06 ± 0.00		0.05 ± 0.00		
68 165	0.01 ± 0.01		0.01 ± 0.02		0.02 ± 0.00		
69 253	0.27 ± 0.04	58	0.22 ± 0.02	50	0.22 ± 0.03	50	BM

Table 4 – *continued*

pgc	Q_H	r_H (arcsec)	Q_J	r_J (arcsec)	Q_K	r_K (arcsec)	Comment
69 327	0.14 ± 0.03	45	0.10 ± 0.01	33	0.11 ± 0.01	53	S
71 047	0.12 ± 0.02		0.07 ± 0.01		0.09 ± 0.00		
72 060	0.20 ± 0.00	13	0.23 ± 0.00	13	0.22 ± 0.00	13	BM

Notes. S= Q_T caused by spiral arms; B = bar-like 'butterfly' structure, but no clear Q_T maximum in the assumed bar region; BM = both Q_T maximum and bar-like butterfly structure appear.

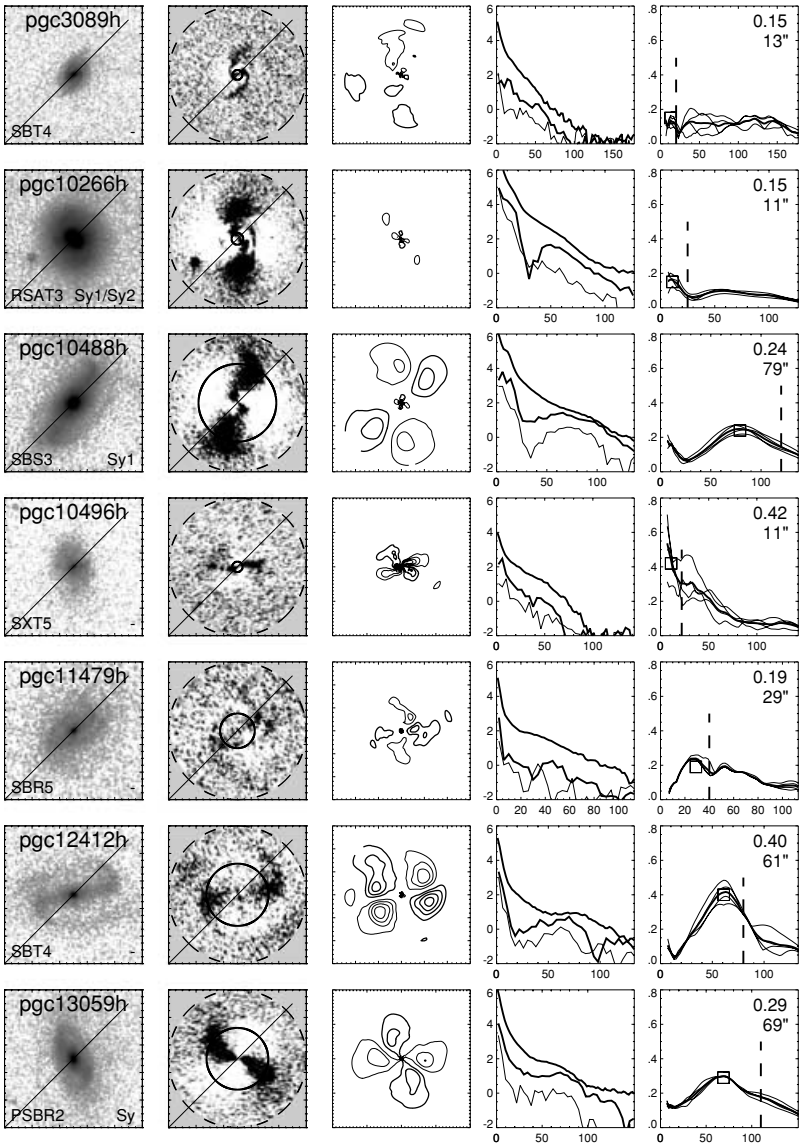

Figure 7. For the 'classical barred' galaxies in the near-IR we show: the original 2MASS image in the plane of the sky (first column), the same image de-projected to face-on orientation, with the $m = 0$ Fourier component being subtracted (second column), the 'butterfly pattern' (third column), the $m = 0$, 2, 4 surface density profiles (fourth column) and the radial Q_T profile (fifth column). The 'butterfly patterns' were calculated from the potentials using all even and odd components up to $m = 6$, while in the Q_T profiles all even components up to 10 were included. In the butterfly diagrams the thick contours correspond to Q_T levels of 0.1, 0.2, 0.3, 0.4, 0.5, while the thin contours refer to corresponding negative levels. In the Q_T profiles the thin lines show measurements in the four image quadrants, whereas the thick lines show the mean values. The dashed vertical line in the Q_T profile shows the length of the bar estimated from the phases of $m = 2$ and 4 density components as explained in the text. The numbers in the upper right-hand corner give the values for the maximum Q_T in the bar region and its radial distance. The maximum is also shown by the box symbol in the Q_T profiles. In the de-projected image the solid circle indicates the location of the maximum Q_T and the dashed circle indicates the measurement region.

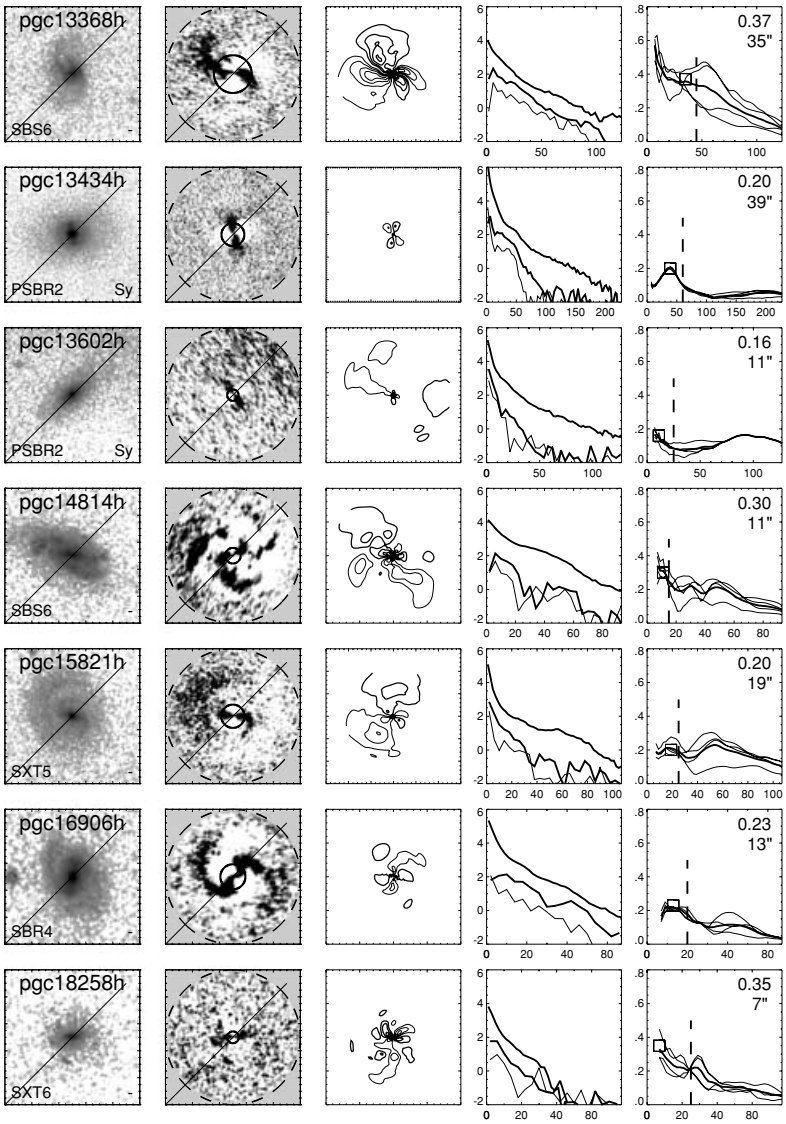

Figure 7 – *continued*

5 CALCULATION OF THE NON-AXISYMMETRIC FORCES FOR THE SAMPLE

5.1 Observed parameters in the potential evaluation

As discussed in the previous section, several approximations were made while calculating the gravitational potential, largely following BB. The main assumption was that the mass-to-luminosity ratio (M/L) is constant throughout the disc. This assumption was made for simplicity, because otherwise possible M/L variations along the disc should be known for each individual galaxy. The studies of colour gradients in galaxies have shown that the central regions of the discs are often redder than the outer discs, which actually suggests larger stellar M/L ratios in the inner discs (Bell & de Jong 2001). Another indicator of a possible non-constancy of the M/L ratio comes from the comparison of the optical surface photometry with the surface mass densities obtained from the rotation curves, showing that the M/L ratio may vary along the disc (Takamiya & Sofue 2000). However, it is possible that the M/L ratio is rather constant in the bar region (see Quillen et al. 1994), in which case the assumption should be reasonably good.

In the evaluation of the barred potential a model for the vertical mass distribution was assumed. The most commonly used models are the exponential and isothermal functions, both being physically justified. An isothermal density function is expected if stars, once formed, do not interact with the other components of the galaxy. Stellar populations of different ages can then be understood as quasi-independent components with different velocity dispersions (Dove & Thronson 1993) so that a more complete picture would be achieved by assuming a superposition of a large number of isothermal sheets with different h_z (Kuijken 1991). On the other hand, if gas settles into an equilibrium prior to star formation or considerable heating of the disc has occurred during the life of a galaxy, an exponential density profile is expected (Burkert & Yoshii 1996). However, empirically the two functions are difficult to distinguish, because the density functions look similar at large vertical heights, whereas near to the galactic plane the evaluation of the density function is complicated by the effects of dust. For the vertical density

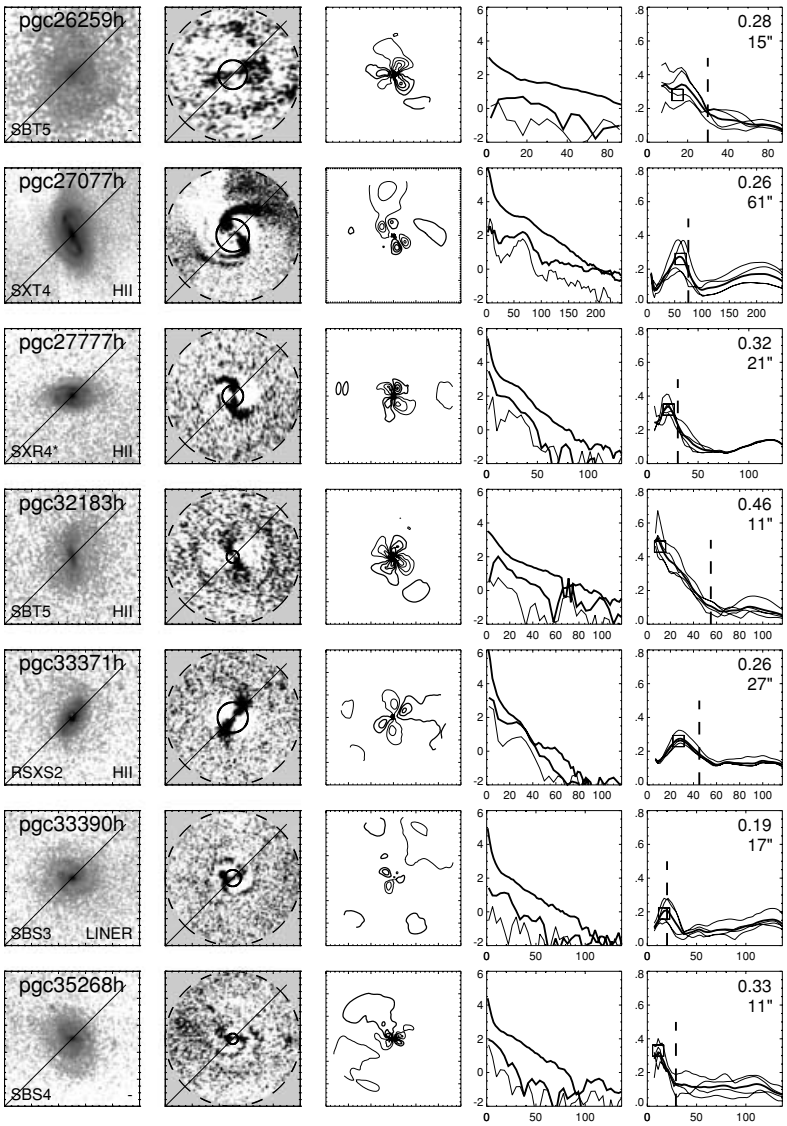

Figure 7 – *continued*

distribution we used an exponential function. However, based on the discussion in Section 4.1, the uncertainty in the vertical model function should have a fairly small influence on the derived forces.

For bar strength measurements, the thickness of the disc is more critical. It has been found to depend on the morphological type of the galaxy (de Grijs 1998) and also to correlate with the radial scalelength of the disc (Wainscoat, Freeman & Hyland 1989; van der Kruit 1988). For early-type galaxies we used $h_r/h_z = 2.5$, and for late-type systems $h_r/h_z = 4.5$. For h_r we use the optical V-band scalelengths from Baggett, Baggett & Anderson (1998), and if not available, they were estimated from the 2MASS images by us. Optical scalelengths were used, but they are expected to be rather similar with those in the near-IR: namely using the bulge-to-disc decompositions given by de Jong (1996) for 186 spiral galaxies, we found that the scalelengths in the V band deviate on average by only 5 per cent from those in the K band. For three of the galaxies, pgc 10266, 15821 and 40097, the scalelengths by Baggett et al. were judged unrealistic: for two of the galaxies they were rather measures of the brightness slopes in the bulge region and for one galaxy the given scalelength represented the outermost very shallow part of the disc, while we are interested in the disc under the bar. Therefore, also for these three galaxies the scalelengths were estimated from 2MASS images.

Bars and bulges often have rather complex structures and may in some cases be difficult to distinguish from each other. For example, 45 per cent of all galaxies (SO–Sd) may have boxy or peanut-shaped bulges or bars, having vertical disc profiles that become thicker towards the outer parts of the discs (Lutticke, Dettmar & Pohlen 2000; Schwarzkopf & Dettmar 2001). These gradients are pronounced in early-type galaxies, but generally do not appear in late-type galaxies. The boxy/peanut structures are often thought to be bulges, but recent observations rather support the idea that they are more likely the thick parts of the bars. This interpretation is also supported by the simulations by Athanassoula (2002), who has shown that boxy/peanut structures are formed from the particles of the discs or bars during the evolution of the galaxy. In this work we have made the simplified assumption that h_z is constant throughout the disc, although the effect of the thickening of the

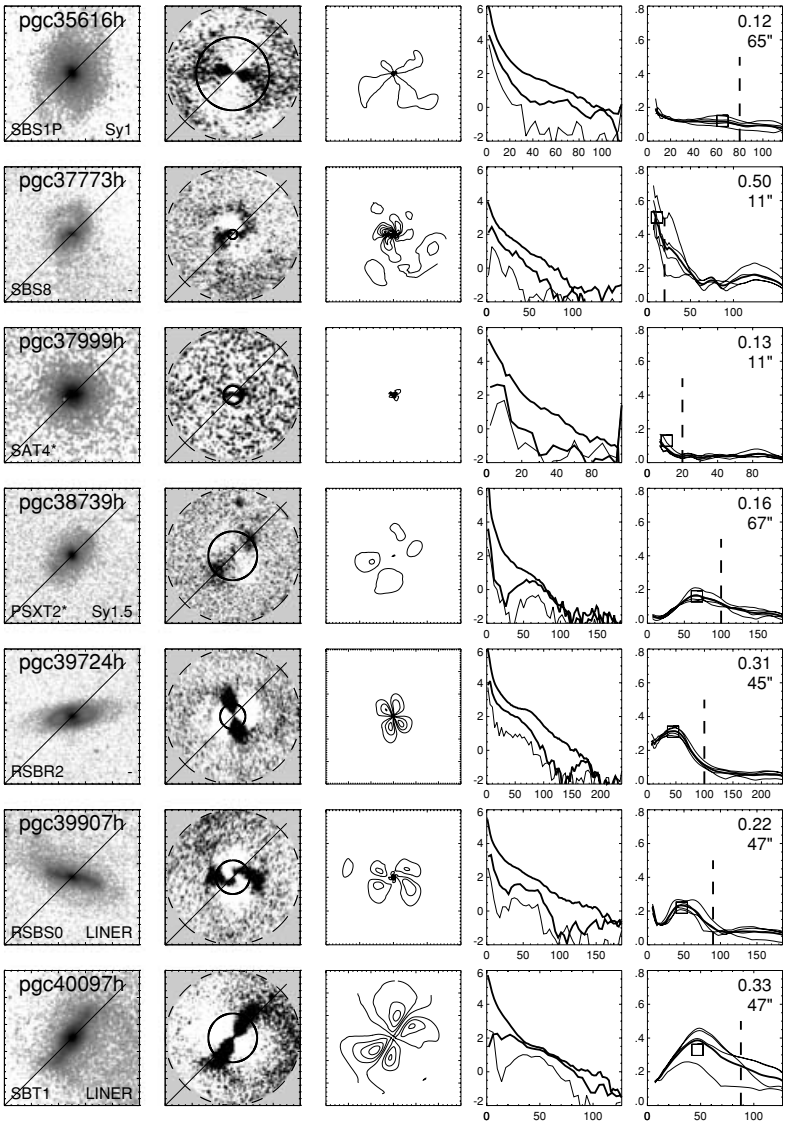

Figure 7 – *continued*

disc toward the outer parts of the disc is also investigated. In the test we used a dh_z/dr gradient of 0.05, typical for normal SO/a galaxies (Schwarzkopf & Dettmar 2001). Galaxy interactions and mergers of small satellite galaxies can also be efficient in thickening the disc, especially in the outer parts of the galaxies (Toth & Ostriker 1992; Walker, Mihos & Hernquist 1996). In fact, observations by Schwarzkopf & Dettmar have shown that the vertical heights of the discs for interacting galaxies can be twice as large as for non-interacting galaxies. Bulges were assumed to be as flat as the discs, which is also a simplified assumption, but may still be valid for the triaxial bulges of SB galaxies (Kormendy 1982, 1993). Evidently, the treatment of bulges needs to be improved in the future.

5.2 Calculation of forces for sample galaxies

As a data base *JHK* images of the 2MASS survey were used. The spatial resolution of the images is 1 arcsec, and the image quality is generally best in the *H* band. Our procedure of estimating the non-axisymmetric forces consisted of the following steps: (i) cleaned sky-subtracted mosaics were constructed; (ii) galaxies were de-projected to face-on orientation; (iii) the images were rebinned by a factor of 2; (iv) Fourier decomposition of the surface density was calculated, and barred potentials were evaluated using the even components up to $m = 6$; (v) the tangential ($F_{\rm T}$) and the mean axisymmetric radial forces ($\langle F_{\rm R}\rangle$) were calculated; and finally (vi) maps of the force ratios were constructed:

$$Q_{\rm T}(r,\phi) = F_{\rm T}(r,\phi)/\langle F_{\rm R}(r,\phi)\rangle. \qquad (14)$$

For a bar the map shows four well-defined regions where the force ratio reaches a maximum or minimum around or near the end of the bar. As in BB, we call this structure a 'butterfly pattern'.

The field of view in the 2MASS images is relatively small and also a large fraction of the galaxies in our sample are quite nearby objects, so that mosaics of two to five images were generally made. The image quality was not as good in the borders as in the central parts of the frames, which in principle, could seriously affect the quality of the mosaics in the regions of interest. For the most nearby

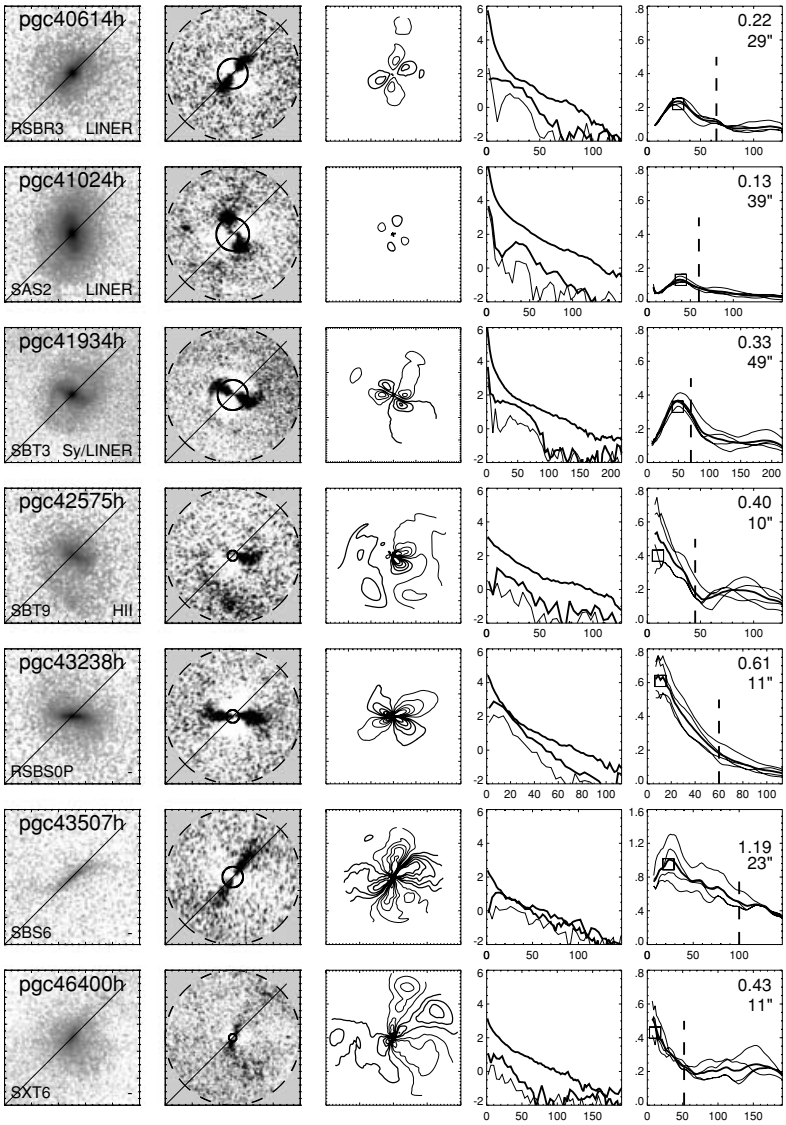

Figure 7 – *continued*

galaxies this was not a problem, because the S/N ratio was high in all parts of the images. For the distant objects the problem was solved so that we never combined images if their borders appeared in the bar region or in the central parts of the galaxies. Before combining the images the overscan regions were removed and the sky values given in the image headers were subtracted. The background levels of the frames were then refined to obtain similar count levels in the galaxy regions in the combined images. Positioning of the frames in the mosaics was performed using stars common in the combined images. Finally, the foreground stars and bad pixels were rejected.

The cleaned (mostly mosaics) images were de-projected to face-on orientation using the position angles (PA) and inclinations (INC) of the discs given in Table 2. In the table some other properties of the galaxies such as the mean revised morphological type T_m, the blue apparent magnitude $B_{\rm T}$, the type of nuclear activity and the scalelength of the disc h_r are also shown. The orientation parameters, the morphological types and the apparent magnitudes are from RC3 if not otherwise mentioned. For some of the galaxies, instead of using the orientation parameters from RC3, they were estimated from the Digitized Sky Survey plates by us. For example, for pgc 18258 the surface brightness contours are clearly affected by the superposition of a small companion, which has not been taken into account in RC3. For the galaxies that had no estimation of PA in the literature, but the discs were in nearly face-on orientation, we used INC $= 0$. In order to estimate the axisymmetric radial forces properly, the bulges were not subtracted.

The maxima of the non-axisymmetric forces, $Q_{\rm b}$, and their radial distances, $r_{Q_{\rm b}}$, are shown in Tables 3 and 4, measured in the J, H and K bands. The uncertainties attached in the tables are the maximum deviations between the four image quadrants. However, the largest uncertainty (see Section 4.1) is caused by the observed scatter in h_r/h_z within each morphological type, which for example for Sc galaxies induces an uncertainty of approximately 15 per cent in $Q_{\rm b}$. Non-axisymmetric forces are also sensitive to the orientation parameters of the galaxies: BB estimated that an uncertainty of ± 10 per cent in the inclination and position angle can induce an uncertainty of two bar strength classes (one bar strength class

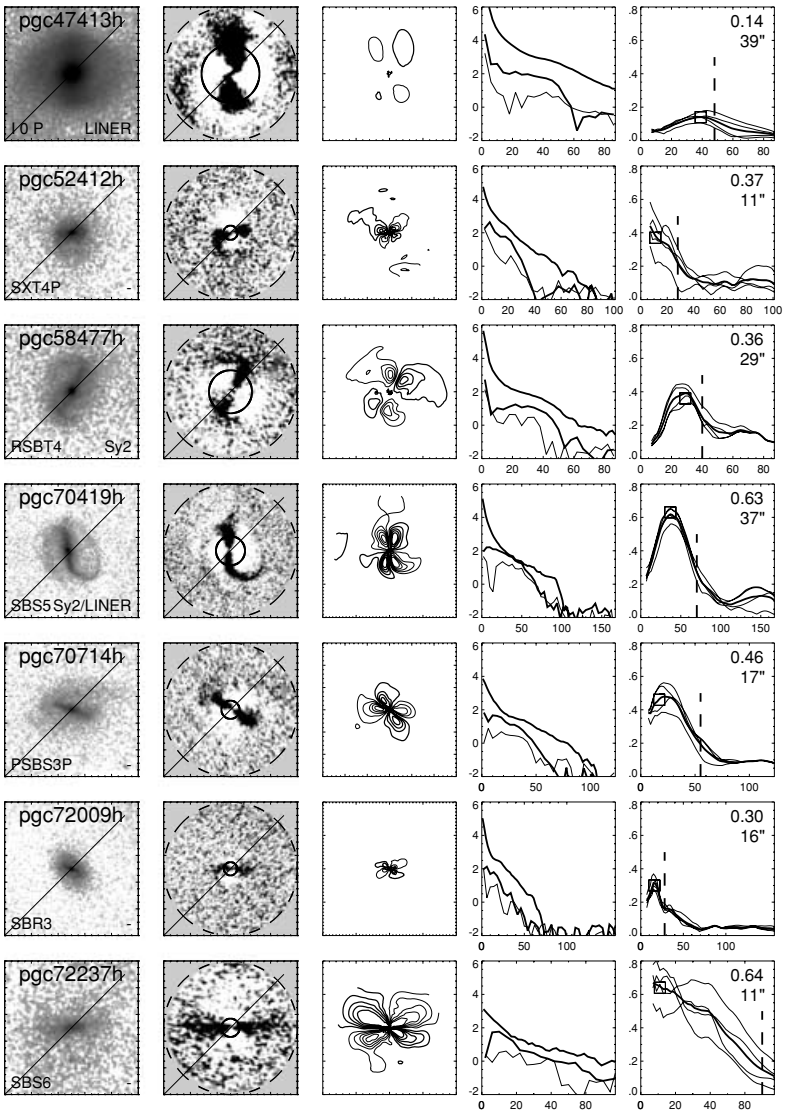

Figure 7 – *continued*

corresponds to 0.1 units in Q_b). Indeed, in future this work can be improved when accurate position angles and inclinations will be available for all of the galaxies studied. Especially for interacting galaxies, the photometric orientation parameters are generally determined from warped or distorted outer discs so that the kinematic observations for them give more reliable values. For example, for M51 the kinematically (Tully 1974) and photometrically (Spillar et al. 1992) estimated inclinations deviate by $\sim 20^\circ$, and for IC 4214 by 10° (Buta et al. 1999), for which the difference can be explained by the bar potential (see Salo et al. 1999). On the other hand, the uncertainty caused by the vertical model (exp versus sech^2) is negligible for thin discs and only approximately 5 per cent for thick discs. Also, the number of Fourier modes or the size of the measurement region do not affect Q_b significantly, if large enough measurement regions ($r_{max} > 2r_{Q_b}$) and enough Fourier modes (even modes up to $m = 6$) are used. The effect of the boxy/peanut-shaped structures in terms of increasing vertical scaleheight towards the outer parts of the discs also appeared to be insignificant for the bar strength.

5.3 Identification of bars and calculation of bar ellipticity

Bars in the near-IR were identified by Fourier techniques. In distinction with bars in general, we use the term 'classical bars' to describe the morphological structures with the ratio of the Fourier amplitude A_2/A_0 larger than 0.3, and with the $m = 2$ phase maintained nearly constant in the bar region (Table 3). For these bars the $m = 4$ amplitudes are also pronounced, there is a clear maximum in the Q_T profile in the bar region and the 'butterfly pattern' shows four regular structures. The Q_T profiles and the 'butterfly patterns' for these galaxies are shown in Fig. 7, also showing the $m = 0$, 2 and 4 surface brightness profiles. The length of the region with a constant $m = 2$ phase was taken to be a measure of the bar length. Both the $m = 2$ and 4 phases are maintained nearly constant in the bar region, but in some cases the $m = 4$ amplitude drops at a slightly shorter distance, in which case we used the mean length of the constant $m = 2$ and 4 phases as the bar length.

In addition to the 'classical bars', other bar-like structures and non-axisymmetries are identified in many of the galaxies in our sample. Actually, the large majority of galaxies have non-axisymmetric

forces, manifested as maxima in the Q_T profiles, whereas in 20 per cent no non-axisymmetric forces were detected above the background level ($Q_b = 0.01$–0.1). Owing to differences in image quality, no single minimum Q_b-value defines the bar-like potential. The non-axisymmetric forces presented in Table 4 deviate from the 'classical bars' in the sense that the $m = 2$ phase is not maintained constant in the assumed bar region and the regular 'butterfly patterns' do not necessarily appear in the force field. In 15 per cent of the galaxies in our sample the Q_T maxima are manifestations of strong spiral arms in the outer parts of the galactic discs.

As discussed by BB, both spherical and flattened bulges can affect the Q_b measurements: in the case of an intrinsically spherical bulge, the effect of assuming a bulge as thin as the disc is to overestimate the axisymmetric radial force and consequently to underestimate the relative bar strength. On the other hand, while de-projecting the image to face-on orientation bulges might cause artefacts in the direction of the minor-axis of the disc. The problem of large bulges was avoided here by limiting to those cases where the maximum tangential force appeared outside the bulge region. The small bulges still make it difficult to detect mini-bars, but by subtracting the $m = 0$ component and by taking into account the de-projection effects, mini-bars could be detected for pgc 10488, 33371, 37999, 40153 and 43495, previously also identified by Buta & Crocker (1993), Pérez-Ramirez et al. (2000), Knapen et al. (1995) and by Block et al. (1994).

Based on the analytical work by Athanassoula (1992) the maximum ellipticity of a bar can be used as an approximation of the bar strength, and its radial distance as an estimate of the bar length. We calculated the ellipticity profiles using a method described in Laurikainen & Salo (2000) in which ellipses were iteratively fitted to the isophotes of the surface brightnesses. The maximum ellipticities ϵ and their radial distances r_ϵ in the bar region for the 'classical bars' are shown in Table 3. In Laurikainen et al. (2002) these ellipticity measurements were utilized to show a good correlation between Q_b and ϵ.

6 THE SAMPLE BIASES

The measurements reported in this work are used to compare bar strengths of the active and non-active galaxies (Laurikainen et al. 2002), so that it is important to study possible biases between different subgroups in the sample.

Active galaxies in our sample appeared to be somewhat brighter than the non-active systems, which is illustrated in Fig. 8(a), also showing a weak correlation between the bar length and the absolute blue magnitude M_B, of the galaxy. However, while scaling the bar length to the scalelength of the disc, the bias was largely diluted (Fig. 8b). A similar correlation has been found previously by Kormendy (1979) for optically measured bar lengths. Owing to the magnitude bias longer bars may have been selected for the active galaxies in our sample. However, we confirmed that this bias does not affect the mean bar strengths in the compared subsamples. This was checked by dividing the non-active galaxies into two magnitude bins with M_B larger and smaller than -19.8 mag, resulting in practically identical mean forces, $\langle Q_b \rangle = 0.22 \pm 0.10$ and 0.24 ± 0.12, respectively (the uncertainties indicate the sample standard deviations).

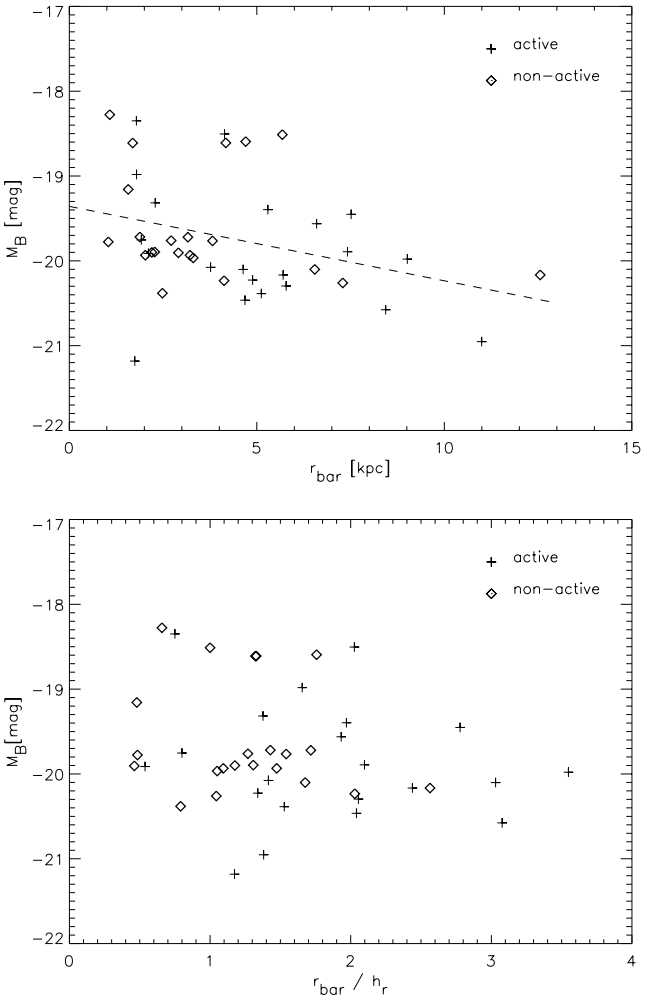

Figure 8. Absolute blue magnitude versus bar length. The magnitudes are from RC3 and bar lengths are estimated from the phases of the $m = 2$ Fourier amplitudes as explained in the text. In the upper panel (a), bar lengths are given in absolute units, using the distances from Tully (1988), and in the lower panel (b) they are scaled to the scalelength of the disc, $H = 75$ km s^{-1} Mpc^{-1}.

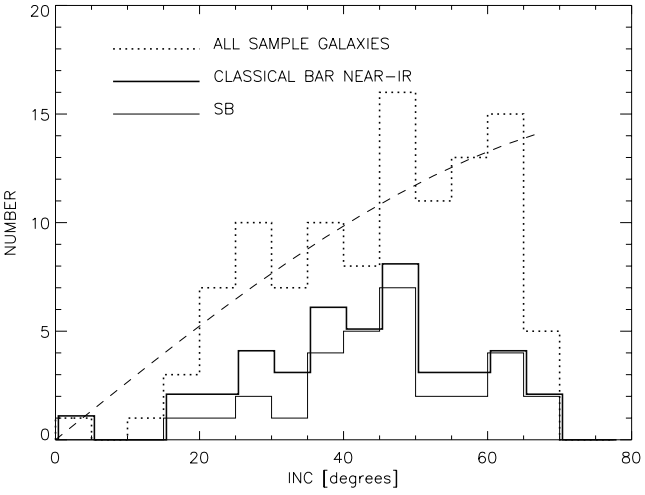

Figure 9. The inclination distribution of the galaxies in our sample, SB galaxies and the 'classical bars' identified in the near-IR (see the text) being shown separately. For comparison, the inclination distribution for all galaxies in our sample is also shown. The dashed line indicates a random distribution of inclinations, normalized to the maximum inclination and the number of galaxies in the sample.

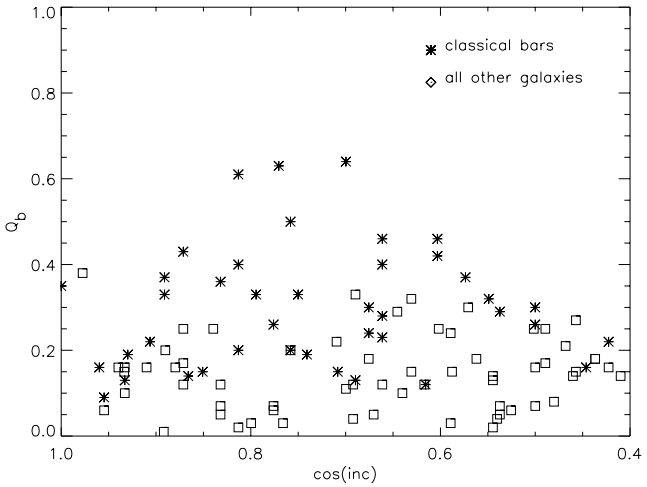

Figure 10. A correlation between the inclination of the disc (INC) and bar strength (Q_b) for the galaxies in our sample.

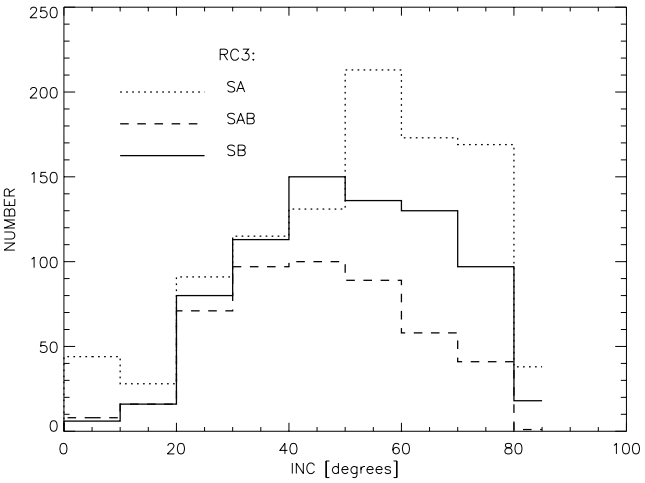

Figure 11. A similar figure to Fig. 9, but shown for the de Vaucouleurs' (1963) classes SA, SAB and SB for a magnitude-limited sample ($B_T < 15.5$ mag) from RC3.

The relative number of barred galaxies drops rapidly in our sample when the inclination of the disc is larger than 50° (see Fig. 9). This is the case both for SAB and SB galaxies and for the 'classical bars' identified in the near-IR. The inclination distribution for the galaxies over the whole sample largely follows a random distribution of orientations, $dN/di \sim \sin i$, expected for an unbiased sample. Again, since in Laurikainen et al. we compare bar strengths between different subsamples it is important that this inclination bias does not affect the mean Q_b-values. It appeared that Q_b does not correlate with the inclination of the disc (see Fig. 10). In particular, for the galaxies with no 'classical bars' Q_b is similar for all inclinations. For the galaxies with 'classical bars' there may be a lack of strong bars among the nearly face-on galaxies (INC < 25°) and clearly among the highly inclined galaxies (INC > 60°), which is probably a manifestation of the uncertainties in the inclination determinations.

In order to check whether the dependence of the bar detection frequency on the inclination is specific for our sample or whether it also appears in larger samples of galaxies, we picked up all galaxies brighter than 15.5 mag from RC3 and constructed histograms for SA, SAB and SB galaxies (Fig. 11), similar to those in Fig. 9. Evidently, a similar bias appears also in RC3: for SA galaxies the inclinations are well sampled to 60°, for SB galaxies to 50° and for SAB galaxies the limit of well-sampled galaxies is even lower than that. Quite surprisingly, the number of SAB galaxies at inclinations larger than 40° drops much more rapidly than the number of SB galaxies, indicating that classification of a galaxy as SAB is very ambiguous. It also seems that in RC3 there is a deficiency of galaxies with very low assigned inclinations (less than 20°), supporting the above interpretation that the lack of strong bars in nearly face-on galaxies is solely caused by uncertainties in the orientation parameters. The inclination bias found might be of importance for example when bar frequencies are compared between low- and high-redshift galaxies. In order to study a possible redshift dependence of the bias, barred galaxy fractions in two inclination bins were compared at two magnitude intervals in RC3. The bias was found to become more significant toward the fainter galaxies. The relative number of SB galaxies with INC > 50° dropped from 32 per cent to 25 per cent while going from the magnitude interval $B_T < 12$ mag to $B_T = 13.5$–14.5 mag, whereas the relative SB galaxy numbers with INC < 50° were identical (38 per cent) in the two magnitude intervals. This means that when bar frequencies at high and low redshifts are compared, bar frequencies of distant galaxies are easily underestimated.

7 COMPARISON OF OPTICAL AND NEAR-IR BARS

The distributions of the non-axisymmetric forces among the de Vaucouleurs' (1963) optical classes SA, SAB and SB are shown in Fig. 12 in J, H and K bands. In agreement with BB and Block et al. (2001), the overlap between the different de Vaucouleurs' types is significant. Based on estimating the ellipticities of bars, a somewhat different result was obtained by Abraham & Merrifield (2000), who argued that SB galaxies are clearly separated from SA and SAB galaxies in bar strength. In our sample SA and SAB galaxies have fairly similar non-axisymmetric forces, the only difference being that some SA galaxies have no non-axisymmetric forces.

Actually, it seems that SB galaxies can belong to any of the bar strength classes from 1 to 6, as defined by BB. In our sample the minimum $Q_b = 0.09$ for SB galaxies is largely as a result of the image quality. We find that bars in SB galaxies are very similar to the 'classical bars' in the near-IR: namely 95 per cent of all SB galaxies in our sample are classified as 'classical' in the near-IR. They also have very similar bar strength distributions in Fig. 12. However, there are 30 per cent more 'classical bars' than SB bars, the excess being distributed to all bar strengths, which means that even strong bars can be hidden by dust in the optical region. In addition to bars, significant tangential forces can also be induced by the spiral arms, especially in the outer parts of the discs, of which M51 (pgc 47404) is a good example. The spiral-related forces may in some cases even amount to $Q_b = 0.26$, corresponding to a bar strength of Class 3. This is quite interesting, because it means that even spiral arms can induce non-axisymmetric forces of the level typically associated with moderately strong bars. These non-axisymmetries may have important implications in secular evolution in galaxies, such as for example for the onset of near nuclear star formation.

8 CONCLUSIONS

Non-axisymmetric forces are calculated for 107 spiral galaxies in J, H and K bands using a method where gravitational potentials are

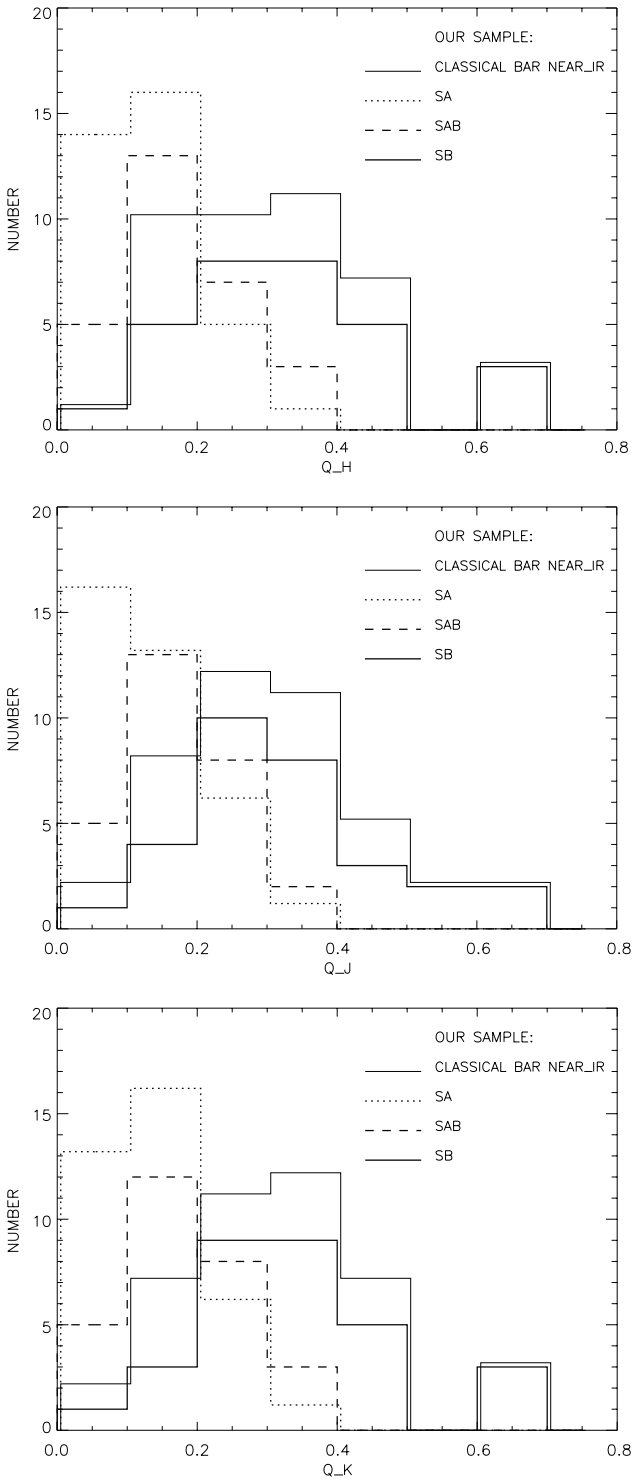

Figure 12. Distribution of the non-axisymmetric forces among the de Vaucouleurs' (1963) classes SA, SAB and SB, measured in J, H and K bands (upper, middle and lower panels, respectively). For comparison, bar strength distribution is shown also for the 'classical bars' identified in the near-IR. Note that not all non-axisymmetric forces in the figure are associated to bar-like potentials, being caused by spiral arms for some SA and SAB galaxies.

evaluated on a polar grid. A non-softened convolution function is applied and the vertical distribution of matter is approximated by an exponential function. The vertical scaleheight of the disc is taken to be a certain fraction of the radial scalelength of the disc, and this ratio is assumed to be larger for the early-type than for the late-type galaxies. The M/L ratio is assumed to be constant throughout the disc. The vertical mass distribution is generally assumed to obey the same formula everywhere in the galaxy, but tests were also performed to estimate the effect of radially non-constant vertical thickness. The phases of the Fourier density amplitudes are used to estimate the lengths of the bars. One of the main concerns of this study is to verify that the different methods of calculating the gravitational potential give mutually consistent results, most of the tests being carried out using a high-quality H-image of NGC 1433 (Buta et al. 2001). In comparison with BB our method is more suitable for weak and noisy images. Also, it is possible to limit to just even Fourier decompositions, which are most likely to characterize the non-axisymmetry related to the bar. Likewise in the polar method it is easy to study distant-dependent h_z. The isophotal ellipticities of bars are also estimated, to facilitate comparisons with bar strengths estimated from maximal forces.

The main results are as follows.

(i) Cartesian and polar grid methods for the potential evaluation are compared. In the Cartesian method the image is sampled on a density array and then a 2D FFT in Cartesian coordinates is applied. In the polar grid method Fourier decomposition of density is calculated on a polar grid using a FFT in azimuth and a direct summation over the radius. We found that similar results are obtained by these two methods for good quality images, provided that enough Fourier components (up to $m = 6$) are included, and the resolution of the Cartesian grid is sufficiently large.

(ii) The bar strength is found to be rather insensitive to the vertical mass model of the disc, as long as a same vertical dispersion is assumed for all models (e.g. $h_{\rm sech2}/h_z = \sqrt{24}/\pi$, $h_{\rm sech}/h_z = \sqrt{8}/\pi$). Boxy/peanut-shaped structures, in terms of non-constant vertical scaleheights along the disc, were also found to be quite unimportant for the evaluation of bar strengths. These parameters affect $Q_{\rm b}$ by less than 5 per cent. The largest uncertainties in $Q_{\rm b}$ are associated with the large scatter in the observed vertical scaleheight of the disc within one Hubble type, and with the observed uncertainties in the orientation parameters of the discs, which both may induce uncertainties of approximately 10–15 per cent in $Q_{\rm b}$.

(iii) Significant non-axisymmetric forces ($Q_{\rm b} > 0.05$) are detected in 80 per cent of the galaxies in our sample. In most cases they were interpreted as bar-like features, based on significant $m = 2$ Fourier amplitudes in the bar regions and distinct 'butterfly patterns' in the $F_{\rm T}/\langle F_{\rm R}\rangle$ ratio maps. In 40 per cent of the galaxies 'classical bars' were detected, determined as having $A_2/A_0 > 0.3$ and the $m = 2$ phases maintained nearly constant in the bar region. In some of the galaxies significant non-axisymmetric forces were detected in the outer parts of the discs connected with spiral arms, corresponding to bar strength Class 3.

(iv) We confirm the previous result by BB and Block et al. (2001) showing a large overlap in bar strength between the optical SA, SAB and SB classes. Actually, SB galaxies can belong to any of the bar strength classes between 1 and 6.

(v) We found that 95 per cent of the SB galaxies in our sample belong to the 'classical bars' identified in the near-IR, which means that the bars are similar. In the optical region one-third of the 'classical bars' are not classified as SB. Even bars that are obscured by dust in the optical band and that become dust penetrated in the near-IR, cover all bar classes from 1 to 6, thus indicating that even strong bars can be obscured by dust.

(vi) Bar lengths are estimated from the phases of the $m = 2$ and 4 Fourier components of density, requiring that the phase be

maintained nearly constant in the bar region. The bar length is found to correlate with the galaxy brightness M_B, confirming the previous result by Kormendy (1979) in the optical region.

(vii) The number of SB galaxies in our sample drops rapidly at inclinations $> 50^\circ$. A similar bias appears also in RC3 when limiting to galaxies brighter than 15.5 mag. This bias might have important implications while studying the frequencies of bars at low and high redshifts, especially because the bias increases toward fainter galaxies. Also, at high inclinations the number of SAB galaxies in RC3 drops much more rapidly than the number of SB galaxies, thus being a manifestation of an ambiguous definition of the de Vaucouleurs' SAB class.

ACKNOWLEDGMENTS

We are grateful to Ron Buta for providing us with his *H*-band image of NGC 1433. This publication utilized images from the 2 Micron All-sky Survey, which is a joint project of the University of Massachusetts and the Infrared Processing and Analysis Centre/California Institute of Technology, funded by the National Aeronautics and Space Administration and the National Science Foundation. It also uses the NASA/IPAC Extragalactic Data base (NED), operated by the Jet Propulsion Laboratory in Caltech. We acknowledge the foundations of Magnus Ehrnrooth and the Academy of Finland for significant financial support.

REFERENCES

Abraham R.G., Merrifield M.R., 2000, AJ, 120, 2835
Athanassoula E., 1992, MNRAS, 259, 328
Athanassoula E., 2002, MNRAS, 330, 35
Baggett W.E., Baggett S.M., Anderson K.S.J., 1998, AJ, 116, 1626
Barnaby D., Thronson H.A., 1992, AJ, 103, 41
Bell E.F., de Jong R.S., 2001, ApJ, 550, 212
Block D., Puerari I., 1999, A&A, 342, 627
Block D.L., Wainscoat R.J., 1991, Nat, 353, 48
Block D.L., Bertin G., Stockton A., Grosbol P., Moorwood A.F.M., Peletier R.F., 1994, A&A, 288, 365
Block D.L., Puerari I., Knapen J.H., Elmegreen B.G., Buta R., Stedman S., Elmegreen D.M., 2001, A&A, 375, 761
Burkert A., Yoshii Y., 1996, MNRAS, 282, 1349
Buta R., 1986, ApJS, 61, 631
Buta R., Block D.L., 2001, ApJ, 550, 243 (BB)
Buta R., Crocker D.A., 1993, AJ, 105, 1344
Buta R., Purcell G., Cobb M., Crocker D., Rautiainen P., Salo H., 1999, AJ, 117, 778
Buta R., Ryder S., Madsen G., Wesson K., Crocker D.A., Combes F., 2001, AJ, 121, 225
de Grijs R., 1998, MNRAS, 299, 595
de Grijs R., Peletier R.F., van der Kruit P.C., 1997, A&A, 327, 966
de Vaucouleuors G., 1955, AJ, 60, 126
de Vaucouleuors G., 1963, ApJS, 8, 31
de Vaucouleurs G., de Vaucouleurs A., Corwin H., Buta R., Paturel G., Fougué P., 1991, Third Reference Cataloque of Bright Galaxies, New York, Springer (RC3)
de Jong R.S., 1996, A&A, 313, 45
de Jong R., van der Kruit P.C., 1994, ApJS, 106, 451
Dove J.B., Thronson H.A., Jr, 1993, ApJ, 411, 632
Elmegreen B.G., Elmegreen D.M., 1985, ApJ, 288, 438
Elmegreen B., Elmegreen D., Seiden E., 1989, ApJ, 343, 602
Eskridge P. et al., 2000, AJ, 119, 536
Heraudeau P., Simien F., 1996, A&AS, 118, 111
Ho L.C., Filippenko A.V., Sargent L.W., 1997, ApJ, 487, 591
Hunt L.K., Malkan M.A., 1999, ApJ, 516, 660
Knapen J.H., Beckman J.E., Shlosman I., Peletier R.F., Heller C.H., de Jong R.S., 1995, ApJ, 443, L73
Knapen J.H., Shlosman I., Peletier R.F., 2000, ApJ, 529, 93
Kormendy J., 1979, ApJ, 227, 714
Kormendy J., 1982, ApJ, 257, 75
Kormendy J., 1993, in de Jonghe H., Habing H.J., eds, IAU Symp 153. Galactic Bulges. Kluwer, Dordrecht, p. 209
Kuijken K., 1991, ApJ, 372, 125
Laurikainen E., Salo H., 2000, AAS, 141, 103
Laurikainen E., Salo H., Rautiainen P., 2002, MNRAS, 331, 880
Lutticke R., Dettmar R.J., Pohlen M., 2000, A&A, 362, 435
Malkan M.A., Gorjian V., Tam R., 1998, ApJS, 117, 25
Moles M., Marquez I., Pérez E., 1995, ApJ, 438, 604
Mulchaey J.S., Regan M.W., 1997, ApJ, 482, L135
Ohta K., 1996, in Buta R., Crocker D.A., Elmegreen B.G., eds, ASP Conf. Ser. Vol. 91, Barred Galaxies. Astron. Soc. Pac., San Francisco, p. 37
Pérez-Ramirez D., Knapen J.H., Peletier R.F., Laine S., Doyon R., Nadeau D., 2000, MNRAS, 317, 234
Quillen A.C., Frogel J.A., Gonzalez R.A., 1994, ApJ, 437, 162
Roth J., 1994, AJ, 108, 862
Salo H., Rautiainen P., Buta R., Purcell C.B., Cobb M.L., Crocker D.A., Laurikainen E., 1999, AJ, 117, 792
Sánchez-Portal M., Díaz A.I., Terlevich R., Terlevich E., Mar A.A., Aretxaga I., 2000, MNRAS, 312, 2
Schwarzkopf U., Dettmar R.J., 2001, A&A, 373, 402
Seigar M.S., James P.A., 1998, MNRAS, 299, 672
Sellwood J.A., Wilkinson A., 1993, Rep. Prog. Phys., 56, 173
Smith J., Gehrz R.D., Grasdalen G.L., Hackwell J.A., Dietz R.D., Friedman S.D., 1990, ApJ, 362, 455
Spillar E., Oh S., Johnson P., Wenz M., 1992, AJ, 103, 793
Takamiya T., Sofue Y., 2000, ApJ, 534, 670
Toth G., Ostriker J.P., 1992, ApJ, 389, 5
Tully R.B., 1974, ApJS, 27, 437
Tully R.B., 1988, Nearby Galaxies Catalogue. Cambridge Univ. Press, Cambridge
van der Kruit P.C., 1988, A&A, 192, 117
van der Kruit P.C., Searle L., 1981, A&A, 95, 105
Wainscoat R.J., Freeman K.C., Hyland A.R., 1989, ApJ, 337, 163
Walker I.R., Mihos C., Hernquist L., 1996, ApJ, 460, 121
Yasuda N., Okamura S., Fukugita M., 1995, ApJS, 96, 359

This paper has been typeset from a TEX/LATEX file prepared by the author.